A non-linear three-dimensional pile–soil model for vibratory pile installation in layered media

Tsetas, Athanasios; Tsouvalas, Apostolos; Metrikine, Andrei V.

DOI
10.1016/j.ijsolstr.2023.112202

Publication date
2023

Document Version
Final published version

Published in
International Journal of Solids and Structures

International Journal of Solids and Structures 269 (2023) 112202

Contents lists available at ScienceDirect

International Journal of Solids and Structures

journal homepage: www.elsevier.com/locate/ijsolstr

A non-linear three-dimensional pile–soil model for vibratory pile installation in layered media

Athanasios Tsetas *, Apostolos Tsouvalas, Andrei V. Metrikine

Faculty of Civil Engineering and Geosciences, Delft University of Technology, Stevinweg 1, Delft, 2628 CN, The Netherlands

ARTICLE INFO

Keywords:
Vibratory pile driving
Vibrations of shells
Thin-Layer Method
Perfectly Matched Layers
Harmonic Balance Method
Green's functions
Field tests
Soil–structure interaction

ABSTRACT

This paper presents a computationally efficient model for vibratory pile installation. A semi-analytical finite element (SAFE) model for thin cylindrical shells is derived to represent the pile. The linear dynamic response of the soil medium is described by means of Green's functions via the Thin-Layer Method (TLM) coupled with Perfectly Matched Layers (PMLs) to account for the underlying elastic half-space. Furthermore, the non-linear pile–soil interaction is addressed through a history-dependent frictional interface and a visco-elasto-plastic tip reaction model that can be characterized on the basis of standard geotechnical *in-situ* measurements. The solution to the non-linear dynamic pile–soil interaction problem is based on the sequential application of the Harmonic Balance Method (HBM). The constituent components of the model are first benchmarked against established numerical schemes. Subsequently, model predictions are compared with experimental data collected from field tests. It is demonstrated that the proposed model amalgamates rigorous theoretical elements and promising prediction capabilities in a computationally efficient framework, applicable to engineering practice.

1. Introduction

The global endeavour towards decarbonization of the energy sector has intensified in recent years (Ahmad and Zhang, 2020). As a result, the demand for renewable energy soars in order to accommodate these rapid developments (Papadis and Tsatsaronis, 2020). Amongst the renewables, offshore wind is considered one of the most propitious energy resources, by virtue of its advantages in comparison with other renewable technologies, e.g. resource availability and cost-related maturity as a technology (Esteban et al., 2011). Due to its pivotal role, the share of offshore wind energy has surged over the past decade leading to a constant increase of the size of offshore wind turbines (OWTs), the distance to shore and the water depth of installation (Rodrigues et al., 2015; Ramírez et al., 2020).

Bottom-fixed foundations are primarily used to support OWTs and amongst the available concepts the monopile is the foremost one, corresponding to 81% of all OWT foundations up to date in Europe (Ramírez et al., 2020). The installation of offshore monopiles is most commonly performed by means of impact hammering, due its robustness and efficacy (Merchant, 2019). However, this approach results into significant underwater noise emissions that can be harmful to marine life, ranging from site avoidance to permanent auditory damage (Tsouvalas and Metrikine, 2016). For that purpose, strict regulatory criteria are imposed and costly noise mitigation systems are employed to conform with those (Tsouvalas, 2020). In view of these concerns, as well as the challenges entailed in the continuous size increase of monopiles, it is essential that alternative installation methods with low environmental impact are developed.

Vibratory driving is a well-known and established technique, characterized by low noise levels, short installation time and low costs, that has been used onshore for decades (Rodger and Littlejohn, 1980). During vibratory installation, the pile excitation is induced by the harmonic (or periodic) rotation of eccentric masses, which leads to significantly lower piling loads compared to impact hammering. At present, the offshore wind industry is increasingly adopting vibratory techniques, albeit their use was hindered in the past due to the limited availability of field data. To further accelerate this shift, knowledge gaps and open questions regarding pile drivability, installation efficiency and post-installation effects need to be addressed (Achmus et al., 2020; Tsetas et al., 2020; Gómez et al., 2022).

The available modelling approaches for vibratory pile installation can be broadly divided into two categories. The first category comprises high-fidelity models. In these approaches, computational schemes such as the total Lagrangian (Chrisopoulos and Vogelsang, 2019), the updated Lagrangian (Machaček et al., 2021) and the Coupled-Eulerian Lagrangian formulation (Staubach et al., 2021) have been employed in

* Corresponding author.
E-mail address: a.tsetas@tudelft.nl (A. Tsetas).

https://doi.org/10.1016/j.ijsolstr.2023.112202
Received 4 September 2022; Received in revised form 25 February 2023; Accepted 6 March 2023
Available online 15 March 2023

conjunction with advanced soil constitutive models (e.g. hypoplasticity), whereas the pile is treated as a rigid body. Significant insights can be gained with such approaches, regarding post-installation soil stress state and the mechanisms of vibratory driving. However, the limitations of these models lie in their excessive computational cost, which renders them rather prohibitive for engineering purposes, and the large number of constitutive soil parameters that need to be calibrated. The latter cannot be retrieved by standard *in-situ* measurements, thus such models require additional extensive laboratory testing.

On the other hand, a range of medium-fidelity models exists for vibratory driving, albeit no established approach can be distinguished. One-dimensional (1-D) radial models have been widely used, where the pile is modelled as a rigid body and the soil is discretized into concentric rigid cylinders (Berghe and Holeyman, 2002; Xiao and Ge, 2022). Such an approach disregards the pile flexible motion and precludes the consideration of soil layering. Furthermore, 1-D wave equation models have been adopted from the area of impact piling (Van Dorp et al., 2019; Mazza and Holeyman, 2019). In these approaches, the pile is modelled as a thin rod and the soil reaction is considered through local and frequency-independent mechanical analogues (Buckley et al., 2017). However, these approaches were originally developed for small-diameter piles and their applicability to offshore monopiles has been questioned in terms of pile (Tsetas et al., 2021) and soil reaction modelling (Byrne et al., 2018). It is evident that an engineering-oriented model that captures adequately the mechanics of vibratory installation is essential.

In this paper, a vibratory pile driving model is developed that aims to bridge the gap between medium- and high-fidelity approaches. The former possess multiple empirical components which are based on various simplifications, while the latter are hindered by computational and practical aspects. For that purpose, modelling approaches that can adequately address the physics of the process, while retaining computational efficiency and engineering applicability are indispensable. In this work, the pile is described as a thin cylindrical shell via a semi-analytical finite element (SAFE) approach (Santos et al., 2009; Spada et al., 2020). Furthermore, the linear elastic layered soil medium is modelled by means of the Thin-Layer Method (TLM) (Kausel, 1999), coupled with Perfectly Matched Layers (PMLs) to describe the underlying half-space (de Oliveira Barbosa et al., 2012; Nguyen and Tassoulas, 2018). The Green's functions for ring loads are found in the frequency-space domain and employed in the solution method (Kausel and Peek, 1982). The contact at the pile–soil interface follows a history-dependent Coulomb friction law, while at the tip a visco-elasto-plastic reaction model is used. Subsequently, the coupled problem is solved by means of sequential application of the Alternating Frequency–Time (AFT) Harmonic Balance Method (HBM) (Cameron and Griffin, 1989; Krack and Gross, 2019), leading to a computationally efficient yet accurate scheme. All these elements are integrated into a non-linear dynamic pile–soil interaction model that constitutes the main novel contribution of this paper. Finally, the established model is compared with pile installation data from field tests (Metrikine et al., 2020; Tsetas et al., 2023). The soil parameters are calibrated based on standard *in-situ* geotechnical measurements and installation data from a vibro-driven pile are compared with model predictions, showcasing its full predictive capabilities.

This paper is structured as follows. In Section 2, the SAFE pile model is developed and the Green's functions of the layered half-space are derived via the TLM+PMLs. The method of solution of the coupled problem by means of a sequential AFT-HBM is presented in Section 3. In Section 4, the numerical components of the model are validated and its predictions are compared with field data in Section 5. Conclusively, in Section 6 a brief outline of the present work is given and the relevant findings are discussed.

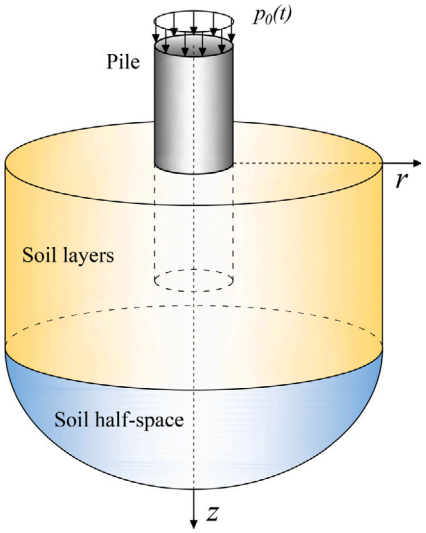

Fig. 1. A pipe pile partially embedded in a layered soil medium.

2. Model description

The present model describes the process of vibratory pile installation. The pile is represented as a thin cylindrical shell and the soil medium as a layered half-space. As regards the input excitation, either a harmonic (or periodic) load can be directly applied at the pile head, or a mechanical analogue of a few degrees-of-freedom (DoFs) can be coupled with the pile by virtue of the finite element-based framework employed (see Section 2.1). In the latter case the harmonic load is applied at a certain component and the overall interaction is taken into account. Considering that all the components of our model are symmetric around the vertical axis, i.e. pile, soil and input excitation, the overall three-dimensional model is axisymmetric and circumferential motion is absent. A schematic of the described model is shown in Fig. 1 and a flowchart that outlines the overall computational framework is presented in Fig. 2.

2.1. A semi-analytical finite element (SAFE) model for thin cylindrical shells

Consider a thin cylindrical shell with wall thickness h_p, length L_p and mid-surface radius R_p as shown in Fig. 3. The thin shell is comprised by linear isotropic elastic material with Young's modulus E_p, Poisson ratio ν_p and mass density ρ_p. The equations of motion for a thin cylindrical shell according to Love–Timoshenko shell theory read (Timoshenko and Woinowsky-Krieger, 1959):

$$\mathfrak{p}_\mathrm{p} + \boldsymbol{\mathcal{L}}_\mathrm{p}\mathbf{s}_\mathrm{p} - \boldsymbol{\mathcal{I}}_\mathrm{p}\mathbf{A}_\mathrm{p}\frac{\partial^2 \mathfrak{u}_\mathrm{p}}{\partial t^2} = \mathbf{0} \tag{1}$$

where the pile displacement/rotation vector $\mathfrak{u}_\mathrm{p}$, the surface forces/moments vector $\mathfrak{p}_\mathrm{p}$ and the force/moment resultants vector $\mathbf{s}_\mathrm{p}$ are defined as follows:

$$\mathfrak{u}_\mathrm{p} = \begin{bmatrix} u & v & w & \beta_z \end{bmatrix}^\mathrm{T}, \quad \mathfrak{p}_\mathrm{p} = \begin{bmatrix} p_{z,\mathrm{p}} & p_{\theta,\mathrm{p}} & p_{r,\mathrm{p}} & m_{z,\mathrm{p}} & m_{\theta,\mathrm{p}} \end{bmatrix}^\mathrm{T} \tag{2}$$

$$\mathbf{s}_\mathrm{p} = \mathbf{S}_\mathrm{p}\mathbf{A}_\mathrm{p}\mathfrak{u}_\mathrm{p} = \begin{bmatrix} N_z & N_\theta & N_{z\theta} & N_{\theta z} & Q_z & Q_\theta & M_z & M_\theta & M_{z\theta} & M_{\theta z} \end{bmatrix}^\mathrm{T} \tag{3}$$

For a cylindrical shell, the two mid-surface circumferences at the shell edges comprise its boundary curves and in case of prescribed tractions the associated boundary conditions read (Leissa, 1973):

$$\mathbf{t}_\mathrm{p}^{(u)} = -\left(\boldsymbol{\mathcal{B}}_\mathrm{p}\mathbf{s}_\mathrm{p}\right)^{(u)}, \quad \mathbf{t}_\mathrm{p}^{(l)} = \left(\boldsymbol{\mathcal{B}}_\mathrm{p}\mathbf{s}_\mathrm{p}\right)^{(l)} \tag{4}$$

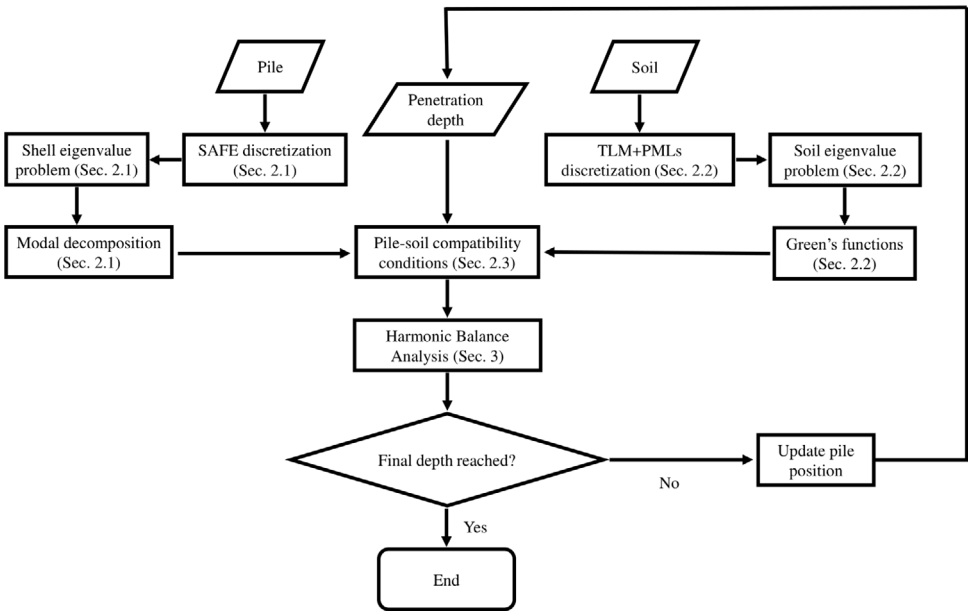

Fig. 2. A flowchart of the present computational framework for vibratory pile installation.

where the superscripts (u) and (l) correspond to the upper ($z = z_u$) and lower ($z = z_l$) shell boundaries, respectively. The differential matrix operators $\boldsymbol{\mathcal{L}}_\mathrm{p}$, $\boldsymbol{\mathcal{I}}_\mathrm{p}$, $\mathbf{S}_\mathrm{p}$ and $\mathbf{A}_\mathrm{p}$ and $\boldsymbol{\mathcal{B}}_\mathrm{p}$ can be obtained from Timoshenko and Woinowsky-Krieger (1959) and will be omitted for brevity. The vector of external forces/moments at the boundary $\mathbf{t}_\mathrm{p}$ reads:

$$\mathbf{t}_\mathrm{p} = \begin{bmatrix} t_{z,\mathrm{p}} & t_{\theta,\mathrm{p}} & t_{r,\mathrm{p}} & t_{zz,\mathrm{p}} \end{bmatrix}^\mathrm{T} \tag{5}$$

In the ensuing, a semi-analytical finite element (SAFE) approach is developed for the vibrations of cylindrical shells. The essence of the method lies in the combination of finite element (FE) discretization in a single coordinate with analytical solutions in the remaining ones and has been successfully applied to laminated composite plates and shells (Bandyopadhyay and Archer, 1979; Taciroglu et al., 2004; Bartoli et al., 2006). In our problem, analytical solutions in θ are combined with an FE discretization in z, resulting into a series of nodal rings (see Fig. 3). First, a cylindrical shell segment is considered with the following assumed solution:

$$\mathfrak{u}_\mathrm{p} = \boldsymbol{\Theta}_n \mathbf{N}_\mathrm{p} \mathbf{x}_\mathrm{p} \tag{6}$$

The diagonal matrix $\boldsymbol{\Theta}_n$ ensures that the response is periodic in θ. Both symmetric and anti-symmetric configurations with respect to $\theta = 0$ are admissible and can be expressed as:

$$\begin{aligned} \boldsymbol{\Theta}_n^\mathrm{s} &= \mathrm{diag}\,\{\cos(n\theta) \quad -\sin(n\theta) \quad \cos(n\theta) \quad \cos(n\theta)\}\,, \\ \boldsymbol{\Theta}_n^\mathrm{a} &= \mathrm{diag}\,\{\sin(n\theta) \quad \cos(n\theta) \quad \sin(n\theta) \quad \sin(n\theta)\} \end{aligned} \tag{7}$$

where the superscripts s and a denote the symmetric and anti-symmetric cases with respect to $\theta = 0$, respectively. The interpolation matrix $\mathbf{N}_\mathrm{p}$ encapsulates the polynomials used to approximate the response of the shell element along the z axis based on the nodal ring values $\mathbf{x}_\mathrm{p}$:

$$\mathbf{N}_\mathrm{p} = \begin{bmatrix} N_1^l(z) & 0 & 0 & 0 & N_2^l(z) & 0 & 0 & 0 \\ 0 & N_1^l(z) & 0 & 0 & 0 & N_2^l(z) & 0 & 0 \\ 0 & 0 & N_1^c(z) & N_2^c(z) & 0 & 0 & N_3^c(z) & N_4^c(z) \\ 0 & 0 & -\dfrac{\mathrm{d}N_1^c(z)}{\mathrm{d}z} & -\dfrac{\mathrm{d}N_2^c(z)}{\mathrm{d}z} & 0 & 0 & -\dfrac{\mathrm{d}N_3^c(z)}{\mathrm{d}z} & -\dfrac{\mathrm{d}N_4^c(z)}{\mathrm{d}z} \end{bmatrix} \tag{8}$$

where the linear Lagrange polynomials $N_1^l(z)$, $N_2^l(z)$ and the cubic Hermite polynomials $N_1^c(z)$, $N_2^c(z)$, $N_3^c(z)$, $N_4^c(z)$ are employed. To derive the SAFE equations, we formulate the principle of virtual work for a cylindrical shell segment and set the virtual work performed by the residuals along the boundary curves and the shell surface equal to zero:

$$\int_0^{2\pi} \left(\left(\delta \mathfrak{u}_\mathrm{p}^{(i)}\right)^\mathrm{T} \mathbf{r}_\mathrm{p}^{(i)} + \left(\delta \mathfrak{u}_\mathrm{p}^{(i+1)}\right)^\mathrm{T} \mathbf{r}_\mathrm{p}^{(i+1)} + \int_{z_i}^{z_{i+1}} \delta(\mathbf{A}_\mathrm{p}\mathfrak{u}_\mathrm{p})^\mathrm{T} \mathbf{r}_{\mathrm{p,S}}\, \mathrm{d}z \right) R_\mathrm{p}\, \mathrm{d}\theta = 0 \tag{9}$$

where $\mathbf{r}_\mathrm{p}^{(i)}$ and $\mathbf{r}_\mathrm{p}^{(i+1)}$ denote the residual force/moment resultants at the shell segment boundaries and $\mathbf{r}_{\mathrm{p,S}}$ denotes the residual surface forces/moments on the shell surface. The aforementioned residuals are expressed as follows:

$$\begin{aligned} \mathbf{r}_\mathrm{p}^{(i)} &= \mathbf{t}_\mathrm{p}^{(i)} + \left(\boldsymbol{\mathcal{B}}_\mathrm{p}\mathbf{s}_\mathrm{p}\right)^{(i)}, \quad \mathbf{r}_\mathrm{p}^{(i+1)} = \mathbf{t}_\mathrm{p}^{(i+1)} - \left(\boldsymbol{\mathcal{B}}_\mathrm{p}\mathbf{s}_\mathrm{p}\right)^{(i+1)}, \\ \mathbf{r}_{\mathrm{p,S}} &= \mathfrak{p}_\mathrm{p} + \boldsymbol{\mathcal{L}}_\mathrm{p}\mathbf{s}_\mathrm{p} - \boldsymbol{\mathcal{I}}_\mathrm{p}\mathbf{A}_\mathrm{p}\frac{\partial^2 \mathfrak{u}_\mathrm{p}}{\partial t^2} \end{aligned} \tag{10}$$

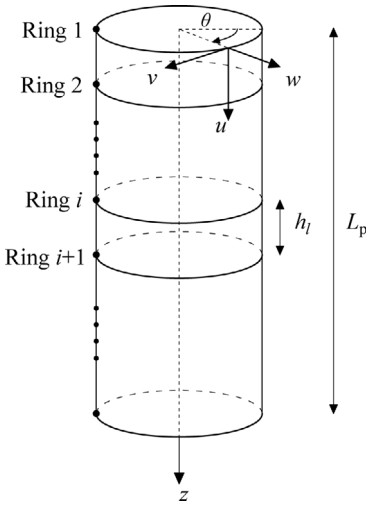

Fig. 3. A thin cylindrical shell with axial discretization into nodal rings based on the SAFE method.

Upon a series of mathematical operations, which are omitted for brevity, the element mass matrix $\mathbf{I}^{l}_{\mathrm{p},n}$, the element stiffness matrix $\mathbf{L}^{l}_{\mathrm{p},n}$ and the vector of consistent forces/moments at the element nodal rings $\mathbf{p}^{l}_{\mathrm{p},n}$ are obtained (see Appendix A):

$$\mathbf{I}^{l}_{\mathrm{p},n} = \int_0^{2\pi}\int_{z_i}^{z_{i+1}} (\mathbf{N}^{\theta}_n)^{\mathrm{T}}\mathbf{A}^{\mathrm{T}}_{\mathrm{p}}\boldsymbol{\mathcal{I}}_{\mathrm{p}}\mathbf{A}_{\mathrm{p}}\mathbf{N}^{\theta}_n R_{\mathrm{p}}\,\mathrm{d}z\mathrm{d}\theta \tag{11}$$

$$\mathbf{L}^{l}_{\mathrm{p},n} = \int_0^{2\pi}\int_{z_i}^{z_{i+1}} \left((\mathbf{N}^{\theta}_n)^{\mathrm{T}}\boldsymbol{\mathcal{B}}_{\mathrm{p}}\mathbf{S}_a\mathbf{A}_{\mathrm{p}}\frac{\mathrm{d}\mathbf{N}^{\theta}_n}{\mathrm{d}z} + \frac{\mathrm{d}(\mathbf{N}^{\theta}_n)^{\mathrm{T}}}{\mathrm{d}z}\boldsymbol{\mathcal{B}}_{\mathrm{p}}\mathbf{S}_a\mathbf{A}_{\mathrm{p}}\mathbf{N}^{\theta}_n - (\mathbf{N}^{\theta}_n)^{\mathrm{T}}\mathbf{A}^{\mathrm{T}}_{\mathrm{p}}\boldsymbol{\mathcal{L}}_{\mathrm{p}}\mathbf{S}_a\mathbf{A}_{\mathrm{p}}\mathbf{N}^{\theta}_n \right) R_{\mathrm{p}}\,\mathrm{d}z\mathrm{d}\theta \tag{12}$$

$$\mathbf{p}^{l}_{\mathrm{p},n} = \int_0^{2\pi} \left(\begin{bmatrix} \boldsymbol{\Theta}^{\mathrm{T}}_n\mathbf{t}^{(i)}_{\mathrm{p}} \\ \boldsymbol{\Theta}^{\mathrm{T}}_n\mathbf{t}^{(i+1)}_{\mathrm{p}} \end{bmatrix} + \int_{z_i}^{z_{i+1}} (\mathbf{N}^{\theta}_n)^{\mathrm{T}}\mathbf{A}^{\mathrm{T}}_{\mathrm{p}}\mathfrak{p}_{\mathrm{p}}\,\mathrm{d}z \right) R_{\mathrm{p}}\,\mathrm{d}\theta \tag{13}$$

where $\mathbf{N}^{\theta}_n = \boldsymbol{\Theta}_n\mathbf{N}_{\mathrm{p}}$ has been introduced for notation compactness. It is remarked that $\mathbf{I}^{l}_{\mathrm{p},n}$, $\mathbf{L}^{l}_{\mathrm{p},n}$ and $\mathbf{p}^{l}_{\mathrm{p},n}$ of the first shell element (pile top) are augmented to account for the pile–device coupling in the case of a mechanical analogue (of few DoFs) describing the vibratory device. The latter enters the formulation via the virtual work performed along the boundary curves, as in standard FE models.

The final SAFE equations are formulated by overlapping all the obtained vectors and matrices in the classical FE sense and rearranging rows and columns to organize by DoFs instead of nodal rings. In that manner the SAFE shell matrices $\mathbf{I}_{\mathrm{p},n}$, $\mathbf{L}_{\mathrm{p},n}$ and vectors $\mathbf{u}_{\mathrm{p},n}$, $\mathbf{p}_{\mathrm{p},n}$ are formed. For an axisymmetric problem ($n = 0$) and in the absence of circumferential motion (symmetric form only), the shell governing equations reduce to:

$$\mathbf{I}^{\mathrm{s}}_{\mathrm{p},0}\frac{\mathrm{d}^2\mathbf{u}^{\mathrm{s}}_{\mathrm{p},0}}{\mathrm{d}t^2} + \mathbf{L}^{\mathrm{s}}_{\mathrm{p},0}\mathbf{u}^{\mathrm{s}}_{\mathrm{p},0} = \mathbf{p}^{\mathrm{s}}_{\mathrm{p},0} \tag{14}$$

To further improve the computational aspects of the model, the modal decomposition is applied in our solution method. The eigenmatrix of the symmetric form for $n = 0$ reads:

$$\boldsymbol{\Phi}^{\mathrm{s}}_{\mathrm{p},0} = \begin{bmatrix} \mathbf{U}^{\mathrm{s}}_0 \\ \mathbf{W}^{\mathrm{s}}_0 \\ \boldsymbol{B}^{\mathrm{s}}_0 \end{bmatrix},\ \mathbf{U}^{\mathrm{s}}_0 = \begin{bmatrix} \mathbf{u}^{\mathrm{s}}_{0,1} & \mathbf{u}^{\mathrm{s}}_{0,2} & \cdots \end{bmatrix},\quad \mathbf{W}^{\mathrm{s}}_0 = \begin{bmatrix} \mathbf{w}^{\mathrm{s}}_{0,1} & \mathbf{w}^{\mathrm{s}}_{0,2} & \cdots \end{bmatrix},\ \boldsymbol{B}^{\mathrm{s}}_0 = \begin{bmatrix} \beta^{\mathrm{s}}_{0,1} & \beta^{\mathrm{s}}_{0,2} & \cdots \end{bmatrix} \tag{15}$$

As can be seen, the circumferential term $\mathbf{V}^{\mathrm{s}}_0$ (equal to zero) is erased for readability in Eq. (15), as well as in all subsequent shell expressions. Finally, the matrix equation that governs the pile modal coordinates $\mathbf{q}^{\mathrm{s}}_0$ reads:

$$\left(\boldsymbol{\Phi}^{\mathrm{s}}_{\mathrm{p},0}\right)^{\mathrm{T}}\mathbf{I}^{\mathrm{s}}_{\mathrm{p},0}\boldsymbol{\Phi}^{\mathrm{s}}_{\mathrm{p},0}\frac{\mathrm{d}^2\mathbf{q}^{\mathrm{s}}_0}{\mathrm{d}t^2} + \left(\boldsymbol{\Phi}^{\mathrm{s}}_{\mathrm{p},0}\right)^{\mathrm{T}}\mathbf{L}^{\mathrm{s}}_{\mathrm{p},0}\boldsymbol{\Phi}^{\mathrm{s}}_{\mathrm{p},0}\mathbf{q}^{\mathrm{s}}_0 = \left(\boldsymbol{\Phi}^{\mathrm{s}}_{\mathrm{p},0}\right)^{\mathrm{T}}\mathbf{p}^{\mathrm{s}}_{\mathrm{p},0} \tag{16}$$

so the pile displacements/rotation $\mathbf{u}_{\mathrm{p}}$ and line load $\mathbf{p}_{\mathrm{p}}$ vectors can be compactly written as:

$$\mathbf{u}_{\mathrm{p}} = \boldsymbol{\Phi}^{\mathrm{s}}_{\mathrm{p},0}\mathbf{q}^{\mathrm{s}}_0,\quad \mathbf{p}_{\mathrm{p}} = \frac{\mathbf{p}^{\mathrm{s}}_{\mathrm{p},0}}{2\pi R_{\mathrm{p}}} \tag{17}$$

As regards the full pile–soil installation model, it is noted that the non-linear soil reaction forces will be introduced as additional loading terms in $\mathbf{p}^{\mathrm{s}}_{\mathrm{p},0}$ (Eq. (14)).

2.2. Wave propagation in a layered medium

2.2.1. Normal modes of a layered medium via the Thin-Layer Method

Consider a soil layer of infinite horizontal extent comprised of a linear elastic isotropic material with mass density ρ_{s} and Lamé constants λ_{s} and G_{s}. The equations of motion in cylindrical coordinates (r, θ, z) can be expressed in matrix form as follows (Kausel, 2006):

$$\mathfrak{p}_{\mathrm{s}} - \rho_{\mathrm{s}}\frac{\partial^2\mathfrak{u}_{\mathrm{s}}}{\partial t^2} + \mathbf{L}^{\mathrm{T}}_{\sigma,\mathrm{s}}\mathbf{D}\mathbf{L}_{\epsilon,\mathrm{s}}\mathfrak{u}_{\mathrm{s}} = \mathbf{0} \tag{18}$$

where the body force vector $\mathfrak{p}_{\mathrm{s}}$ and the displacement vector $\mathfrak{u}_{\mathrm{s}}$ are defined as:

$$\mathfrak{p}_{\mathrm{s}} = \begin{bmatrix} p_{r,\mathrm{s}} & p_{\theta,\mathrm{s}} & p_{z,\mathrm{s}} \end{bmatrix}^{\mathrm{T}},\quad \mathfrak{u}_{\mathrm{s}} = \begin{bmatrix} u_r & u_\theta & u_z \end{bmatrix}^{\mathrm{T}} \tag{19}$$

The differential matrix operators $\mathbf{L}_{\sigma,\mathrm{s}}$ and $\mathbf{L}_{\epsilon,\mathrm{s}}$ and the constitutive matrix $\mathbf{D}$ can be found in Kausel (2006).

For a soil layer bounded by two horizontal planes, the boundary conditions in the presence of external tractions read:

$$\mathbf{t}^{(u)}_{\mathrm{s}} = -\mathbf{s}^{(u)}_z,\quad \mathbf{t}^{(l)}_{\mathrm{s}} = \mathbf{s}^{(l)}_z \tag{20}$$

where the superscripts (u) and (l) correspond to the upper ($z = z_u$) and lower ($z = z_l$) horizontal planes, respectively. The traction vector $\mathbf{t}_{\mathrm{s}}$ and the stress vector along a horizontal surface $\mathbf{s}_z$ are defined as:

$$\mathbf{t}_{\mathrm{s}} = \begin{bmatrix} t_{r,\mathrm{s}} & t_{\theta,\mathrm{s}} & t_{z,\mathrm{s}} \end{bmatrix}^{\mathrm{T}},\quad \mathbf{s}_z = \begin{bmatrix} \sigma_{zr,\mathrm{s}} & \sigma_{z\theta,\mathrm{s}} & \sigma_{zz,\mathrm{s}} \end{bmatrix}^{\mathrm{T}} \tag{21}$$

At this point, we proceed to discretize a vertically inhomogeneous medium (comprised by homogeneous horizontal layers of dissimilar material properties) into thin layers in FE sense, i.e. small compared to the excited wavelengths, according to the Thin-Layer Method (TLM) (Kausel and Roësset, 1981). We begin by assuming that the solution inside a homogeneous thin layer of thickness h_l has the following general form:

$$\mathfrak{u}_{\mathrm{s}} = \mathbf{T}_n\mathbf{C}_n\mathbf{N}_{\mathrm{s}}\mathbf{x}_{\mathrm{s}} \tag{22}$$

In Eq. (22), the diagonal matrix $\mathbf{T}_n$ is an azimuthal matrix expanding the displacement field into a Fourier series in θ. The displacement field may be either symmetric or anti-symmetric with respect to $\theta = 0$, with the corresponding azimuthal matrices defined as:

$$\begin{aligned} \mathbf{T}^{\mathrm{s}}_n &= \mathrm{diag}\left\{\cos(n\theta)\quad -\sin(n\theta)\quad \cos(n\theta)\right\}, \\ \mathbf{T}^{\mathrm{a}}_n &= \mathrm{diag}\left\{\sin(n\theta)\quad \cos(n\theta)\quad \sin(n\theta)\right\} \end{aligned} \tag{23}$$

Furthermore, the Bessel matrix $\mathbf{C}_n$ is defined as follows:

$$\mathbf{C}_n = \begin{bmatrix} \dfrac{\mathrm{d}J_n(kr)}{\mathrm{d}(kr)} & \dfrac{n}{kr}J_n(kr) & 0 \\ \dfrac{n}{kr}J_n(kr) & \dfrac{\mathrm{d}J_n(kr)}{\mathrm{d}(kr)} & 0 \\ 0 & 0 & J_n(kr) \end{bmatrix} \tag{24}$$

where k is the radial wavenumber variable.

The chosen dependencies in the radial and circumferential directions are based on the exact solutions for wave propagation in a solid medium (Kausel, 2006). Finally, the soil displacements are interpolated along z based on the vector of interface values $\mathbf{x}_{\mathrm{s}}$ and the interpolation matrix $\mathbf{N}_{\mathrm{s}}$ which can be expressed as:

$$\mathbf{N}_{\mathrm{s}} = \begin{bmatrix} N^l_1(z)\mathbf{I}_3 & N^l_2(z)\mathbf{I}_3 \end{bmatrix} \tag{25}$$

where $N^l_1(z)$ and $N^l_2(z)$ are linear Lagrange polynomials and $\mathbf{I}_3$ is a 3×3 identity matrix.

By substituting Eq. (22) into Eqs. (18) and (20) and considering that the adopted solution is approximate, residual body forces and surface tractions at the boundaries are generated. By invoking the principle of virtual work and requiring that residual body forces and surface tractions perform virtual work equal to zero, we obtain:

$$\int_0^{+\infty}\int_0^{2\pi}\left(\left(\delta\mathfrak{u}^{(i)}_{\mathrm{s}}\right)^{\mathrm{T}}\mathbf{r}^{(i)}_{\mathrm{s}} + \left(\delta\mathfrak{u}^{(i+1)}_{\mathrm{s}}\right)^{\mathrm{T}}\mathbf{r}^{(i+1)}_{\mathrm{s}} + \int_{z_i}^{z_{i+1}}\delta\mathfrak{u}^{\mathrm{T}}_{\mathrm{s}}\mathbf{r}_{\mathrm{s,V}}\mathrm{d}z \right) r\,\mathrm{d}\theta\,\mathrm{d}r = 0 \tag{26}$$

where $\mathbf{r}_{\mathrm{s,V}}$ is the vector of residual body forces in the interior of the thin layer and $\mathbf{r}^{(i)}_{\mathrm{s}}$, $\mathbf{r}^{(i+1)}_{\mathrm{s}}$ are the vectors of residual surface tractions at the upper ($z = z_i$) and lower ($z = z_{i+1}$) bounding horizontal planes, respectively. The residuals $\mathbf{r}^{(i)}_{\mathrm{s}}$, $\mathbf{r}^{(i+1)}_{\mathrm{s}}$ and $\mathbf{r}_{\mathrm{s,V}}$ are defined as:

$$\mathbf{r}^{(i)}_{\mathrm{s}} = \mathbf{t}^{(i)}_{\mathrm{s}} + \mathbf{s}^{(i)}_z,\quad \mathbf{r}^{(i+1)}_{\mathrm{s}} = \mathbf{t}^{(i+1)}_{\mathrm{s}} - \mathbf{s}^{(i+1)}_z,\quad \mathbf{r}_{\mathrm{s,V}} = \mathfrak{p}_{\mathrm{s}} + \mathbf{L}^{\mathrm{T}}_{\sigma,\mathrm{s}}\mathbf{D}\mathbf{L}_{\epsilon,\mathrm{s}}\mathfrak{u}_{\mathrm{s}} - \rho_{\mathrm{s}}\frac{\partial^2\mathfrak{u}_{\mathrm{s}}}{\partial t^2} \tag{27}$$

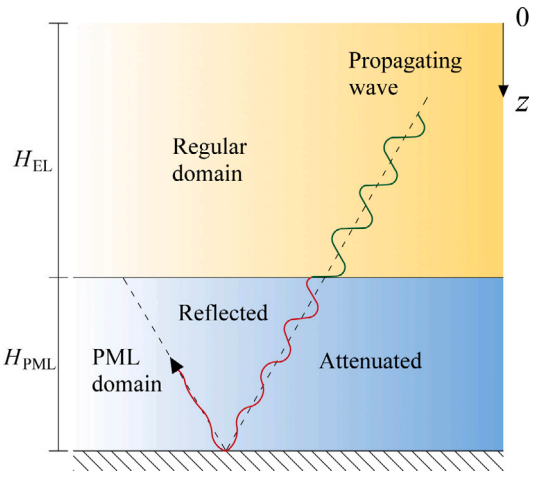

Fig. 4. Attenuation of propagating waves inside the PML region.

In the absence of external body forces and surface tractions, the matrices $\mathbf{A}^l$, $\mathbf{B}^l$, $\mathbf{G}^l$ and $\mathbf{M}^l$ are obtained, which characterize each thin layer l (Kausel and Roësset, 1981). By overlapping all the thin layer matrices in the usual FE sense, the matrices for the layered soil medium are formed. Subsequently, we group the DoFs instead of the layer interfaces by rearranging rows and columns, which leads to the following matrix equation:

$$\left(k^2\mathbf{A}^* + k\mathbf{B}^* + \mathbf{G}^* - \omega^2\mathbf{M}^*\right)\boldsymbol{\phi} = \mathbf{0} \tag{28}$$

where the soil matrices are defined as:

$$\mathbf{A}^* = \begin{bmatrix} \mathbf{A}_r & \mathbf{0} & \mathbf{0} \\ \mathbf{0} & \mathbf{A}_\theta & \mathbf{0} \\ \mathbf{0} & \mathbf{0} & \mathbf{A}_z \end{bmatrix},\ \mathbf{B}^* = \begin{bmatrix} \mathbf{0} & \mathbf{0} & \mathbf{B}_{rz} \\ \mathbf{0} & \mathbf{0} & \mathbf{0} \\ \mathbf{B}_{zr} & \mathbf{0} & \mathbf{0} \end{bmatrix},$$
$$\mathbf{G}^* = \begin{bmatrix} \mathbf{G}_r & \mathbf{0} & \mathbf{0} \\ \mathbf{0} & \mathbf{G}_\theta & \mathbf{0} \\ \mathbf{0} & \mathbf{0} & \mathbf{G}_z \end{bmatrix},\ \mathbf{M}^* = \begin{bmatrix} \mathbf{M}_r & \mathbf{0} & \mathbf{0} \\ \mathbf{0} & \mathbf{M}_\theta & \mathbf{0} \\ \mathbf{0} & \mathbf{0} & \mathbf{M}_z \end{bmatrix} \tag{29}$$

As can be seen, Eq. (28) describes a quadratic eigenvalue problem in k. The special structure of the involved matrices (Eq. (29)) can be exploited and results in two uncoupled generalized linear eigenvalue problems for the normal modes of generalized Rayleigh (SV-P) and Love (SH) waves, respectively. Due to the axisymmetric problem formulation ($n = 0$) and the absence of circumferential motion, only SV-P waves are considered:

$$\left(k^2\bar{\mathbf{A}} + \bar{\mathbf{C}}\right)\begin{bmatrix} \boldsymbol{\phi}_r \\ k\boldsymbol{\phi}_z \end{bmatrix} = \begin{bmatrix} \mathbf{0} \\ \mathbf{0} \end{bmatrix} \tag{30}$$

where the matrices $\bar{\mathbf{A}}$ and $\bar{\mathbf{C}}$ are defined as:

$$\bar{\mathbf{A}} = \begin{bmatrix} \mathbf{A}_r & \mathbf{0} \\ \mathbf{B}_{zr} & \mathbf{A}_z \end{bmatrix},\ \bar{\mathbf{C}} = \begin{bmatrix} \mathbf{G}_r - \omega^2\mathbf{M}_r & \mathbf{B}_{rz} \\ \mathbf{0} & \mathbf{G}_z - \omega^2\mathbf{M}_z \end{bmatrix} \tag{31}$$

2.2.2. Half-space inclusion in the Thin-Layer Method via Perfectly Matched Layers

The approach outlined in Section 2.2.1 is suitable to analyse wave propagation in a layered medium with fixed base (e.g. bedrock). Presently, the Perfectly Matched Layers (PMLs) comprise one of the most successful techniques to describe semi-infinite media with finite computational domains augmented with absorbing boundary layers (Morvaridi and Brun, 2016; Kucukcoban et al., 2019). In the ensuing we outline the coupling of the TLM with PMLs, in order to analyse a layered soil medium underlain by a half-space (de Oliveira Barbosa et al., 2012; Kausel and de Oliveira Barbosa, 2012).

The key principle of PMLs lies in the transformation of the spatial coordinates into complex-valued coordinates by means of complex stretching functions. In our case, the vertical coordinate z is transformed to a complex-valued stretched coordinate $\bar{z}$ as follows:

$$\bar{z} = \int_0^z \varepsilon_s\left(z', \omega\right)\ \mathrm{d}z' \tag{32}$$

where $\varepsilon_s(z, \omega)$ denotes the complex-valued stretching function and in the standard PML formulation has the following form:

$$\varepsilon_s(z, \omega) = \alpha_s(z) + \frac{\beta_s(z)}{\mathrm{i}\omega} \tag{33}$$

where $\alpha_s(z)$ is the scaling function and $\beta_s(z)$ is the attenuation function; the former controls the amplitude decay of evanescent waves, while the latter is responsible for the attenuation of propagating waves (see Fig. 4). Both functions should increase monotonically with z and ensure continuity of the vertical coordinate at the interface between the regular and the PML domain, i.e. $\alpha_s(H_{EL}) = 1$ and $\beta_s(H_{EL}) = 0$ (Kucukcoban and Kallivokas, 2011). The scaling and attenuation functions are customarily expressed as follows (Francois et al., 2021):

$$\alpha_s(z) = \begin{cases} 1, & 0 \le z \le H_{EL} \\ 1 + \alpha_0\left(\dfrac{z - H_{EL}}{H_{PML}}\right)^{m_{PML}}, & H_{EL} \le z \le H_{EL} + H_{PML} \end{cases} \tag{34}$$

$$\beta_s(z) = \begin{cases} 0, & 0 \le z \le H_{EL} \\ \beta_0\left(\dfrac{z - H_{EL}}{H_{PML}}\right)^{m_{PML}}, & H_{EL} \le z \le H_{EL} + H_{PML} \end{cases} \tag{35}$$

where H_{EL} is the thickness of the regular domain, H_{PML} is the thickness of the PML domain and m_{PML} is the degree of the polynomial attenuation inside the PMLs. The scalar tuning parameters α_0 and β_0 control the scaling and attenuation inside the PMLs, respectively.

By employing the stretching function used by Collino and Tsogka (2001) and substituting it in Eq. (32), the complex-valued stretched coordinate $\bar{z}$ is obtained:

$$\bar{z} = z - \mathrm{i}\mathrm{H}(z - H_{EL})\frac{\beta_0 H_{PML}}{\omega(m_{PML} + 1)}\left(\frac{z - H_{EL}}{H_{PML}}\right)^{m_{PML}+1} \tag{36}$$

where $\mathrm{H}(\cdot)$ is the Heaviside function. Consider a PML domain with thickness H_{PML} that is discretized into N_{PML} thin layers of equal thickness. Following the procedure developed by Kausel and de Oliveira Barbosa (2012), PMLs are readily incorporated in the TLM by simply replacing the thickness of the lth thin layer h_l in the PML domain with a complex-valued stretched thickness $\bar{h}_l$, defined as:

$$\bar{h}_l = H_{PML}\left[\frac{1}{N_{PML}} - \mathrm{i}\frac{\beta_0}{\omega(m_{PML} + 1)} \times \left(\left(\frac{l}{N_{PML}}\right)^{m_{PML}+1} - \left(\frac{l-1}{N_{PML}}\right)^{m_{PML}+1}\right)\right], \quad 1 \le l \le N_{PML} \tag{37}$$

It is noted that the introduction of PMLs may lead to spurious modes depending on the size of the PML domain, the thickness of the thin layers inside the PML region, as well as the scaling and attenuation parameters (Kim and Pasciak, 2009; Matuszyk, 2017; Gallezot et al., 2018). To avoid leaking of non-physical energy into the elastic domain, either simple measures such as enlargement of the PML domain may be employed or the spurious modes may be filtered, e.g. based on the ratio of kinetic energy in PML region over the kinetic energy in the whole domain (Treyssede et al., 2014). Without entering into lengthy details, the choice of the scaling and attenuation tuning parameters is based on the recommendations by de Oliveira Barbosa et al. (2012). Conclusively, in our model the layered soil is placed on top of an assembly of PMLs, defined as thin layers with complex-valued stretched thickness, to account for the underlying half-space as shown in Fig. 5.

2.2.3. Green's functions of a layered medium via the Thin-Layer Method

For the problem of our interest, we proceed to derive the Green's functions in the frequency-space domain due to vertical and radial

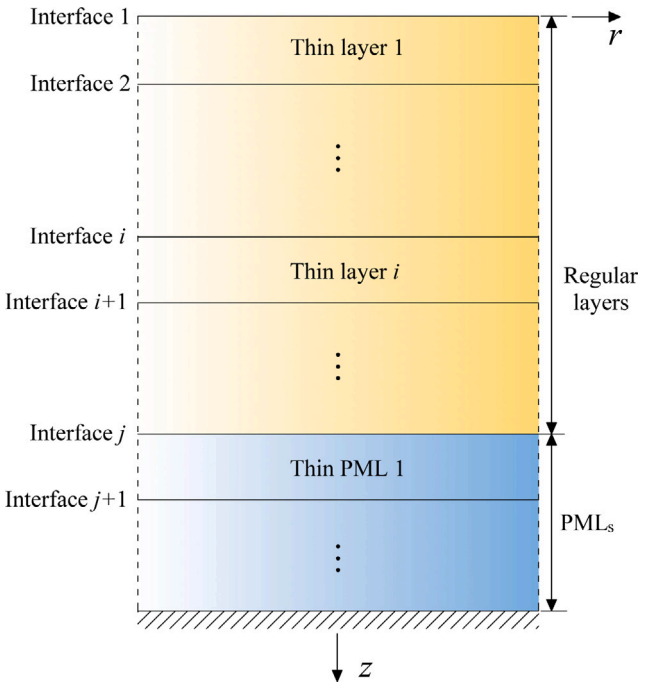

Fig. 5. A layered soil half-space modelled via the TLM+PMLs.

ring loads. First, we define the displacement vector $\widetilde{\mathbf{u}}_{\mathrm{s}}^{(i)}$ at ith elevation (layer interface) in the frequency-space domain:

$$\widetilde{\mathbf{u}}_{\mathrm{s}}^{(i)} = \begin{bmatrix} \widetilde{u}_r^{(i)} & \widetilde{u}_\theta^{(i)} & \widetilde{u}_z^{(i)} \end{bmatrix}^{\mathrm{T}} = \sum_{n=0}^{\infty} \mathbf{T}_n \int_0^{\infty} k \mathbf{C}_n \widehat{\mathbf{u}}_{\mathrm{s},n}^{(i)} \, \mathrm{d}k \tag{38}$$

where $\widehat{\mathbf{u}}_{\mathrm{s},n}^{(i)}$ denotes the displacement vector at elevation z_i in the frequency-(radial–azimuthal)-wavenumber domain. In the ensuing, the symbols $\widetilde{(\cdot)}$ and $\widehat{(\cdot)}$ refer to quantities in the frequency-space and frequency-(radial–azimuthal)-wavenumber domain, respectively. Transformation to the latter can be achieved by means of a discrete Fourier transform in the azimuth θ and a Hankel transform in the radial coordinate r:

$$\widehat{\mathbf{u}}_{\mathrm{s},n}^{(i)} = \begin{bmatrix} \widehat{u}_{r,n}^{(i)} & \widehat{u}_{\theta,n}^{(i)} & \widehat{u}_{z,n}^{(i)} \end{bmatrix}^{\mathrm{T}} = a_n \int_0^{\infty} r \mathbf{C}_n \int_0^{2\pi} \mathbf{T}_n \widetilde{\mathbf{u}}_{\mathrm{s}}^{(i)} \, \mathrm{d}\theta \, \mathrm{d}r \tag{39}$$

where $a_0 = \frac{1}{2\pi}$ and $a_n = \frac{1}{\pi}$ $(n \neq 0)$. The azimuthal matrix $\mathbf{T}_n$ is a placeholder that can be substituted by its symmetric ($\mathbf{T}_n^{\mathrm{s}}$) or anti-symmetric ($\mathbf{T}_n^{\mathrm{a}}$) form, depending on the case considered. For the external load vector, an analogous transformation pair $\widetilde{\mathbf{p}}_{\mathrm{s}}^{(j)}$, $\widehat{\mathbf{p}}_{\mathrm{s},n}^{(j)}$ is defined at the jth layer interface, involving the exact same transformations employed in Eqs. (38) and (39).

A solution in the form of modal superposition is sought, starting from the following relation between external loads and displacements in the frequency-(radial–azimuthal)-wavenumber domain (SV-P):

$$\left(k^2 \bar{\mathbf{A}} + \bar{\mathbf{C}}\right) \begin{bmatrix} \widehat{\mathbf{u}}_{r,n} \\ k \widehat{\mathbf{u}}_{z,n} \end{bmatrix} = \begin{bmatrix} \widehat{\mathbf{p}}_{r,n} \\ k \widehat{\mathbf{p}}_{z,n} \end{bmatrix} \tag{40}$$

where $\widehat{\mathbf{u}}_{r,n}$ and $\widehat{\mathbf{u}}_{z,n}$ are the radial and vertical displacement vectors, respectively. The vectors $\widehat{\mathbf{p}}_{r,n}$ and $\widehat{\mathbf{p}}_{z,n}$ denote the consistent external loads at the layer interfaces, derived according to the TLM.

A series of matrix operations needs to be performed at this point, involving the following orthogonality and normalization relations employed by Waas (1972) and Kausel (1981):

$$\mathbf{Y}^{\mathrm{T}} \bar{\mathbf{A}} \mathbf{Z} = \mathbf{K}_{\mathrm{R}}, \quad \mathbf{Y}^{\mathrm{T}} \bar{\mathbf{C}} \mathbf{Z} = -\mathbf{K}_{\mathrm{R}}^3 \tag{41}$$

where $\mathbf{K}_{\mathrm{R}} = \mathrm{diag}\left\{ k_{\mathrm{R},1} \;\; k_{\mathrm{R},2} \;\; \cdots \right\}$ is a diagonal matrix containing the wavenumbers $k_{\mathrm{R},m}$ associated with the Rayleigh modes, which are found by Eq. (30). Furthermore, the matrices $\mathbf{Y}$ and $\mathbf{Z}$ contain the left and right eigenvectors, respectively:

$$\mathbf{Z} = \begin{bmatrix} \boldsymbol{\Phi}_r \\ \boldsymbol{\Phi}_z \mathbf{K}_{\mathrm{R}} \end{bmatrix}, \quad \mathbf{Y} = \begin{bmatrix} \boldsymbol{\Phi}_r \mathbf{K}_{\mathrm{R}} \\ \boldsymbol{\Phi}_z \end{bmatrix}, \tag{42}$$
$$\boldsymbol{\Phi}_r = \begin{bmatrix} \boldsymbol{\phi}_{r,1} & \boldsymbol{\phi}_{r,2} & \cdots \end{bmatrix}, \quad \boldsymbol{\Phi}_z = \begin{bmatrix} \boldsymbol{\phi}_{z,1} & \boldsymbol{\phi}_{z,2} & \cdots \end{bmatrix}$$

where $\boldsymbol{\phi}_{r,m} = \begin{bmatrix} \phi_{r,m}^{(1)} & \phi_{r,m}^{(2)} & \cdots \end{bmatrix}^{\mathrm{T}}$ and $\boldsymbol{\phi}_{z,m} = \begin{bmatrix} \phi_{z,m}^{(1)} & \phi_{z,m}^{(2)} & \cdots \end{bmatrix}^{\mathrm{T}}$ are the vectors of radial and vertical displacements at the layer interfaces for the mth Rayleigh mode. An elaborate description of the intermediate operations can be found in Kausel and Peek (1982), Kausel (1981). Finally, for the SV-P problem the displacements at the layer interfaces in the frequency-(radial–azimuthal)-wavenumber domain can be written as:

$$\begin{bmatrix} \widehat{\mathbf{u}}_{r,n} \\ \widehat{\mathbf{u}}_{z,n} \end{bmatrix} = \begin{bmatrix} \boldsymbol{\Phi}_r \mathbf{D}_{\mathrm{R}} \boldsymbol{\Phi}_r^{\mathrm{T}} & k \boldsymbol{\Phi}_r \mathbf{K}_{\mathrm{R}}^{-1} \mathbf{D}_{\mathrm{R}} \boldsymbol{\Phi}_z^{\mathrm{T}} \\ \frac{1}{k} \boldsymbol{\Phi}_z \mathbf{D}_{\mathrm{R}} \mathbf{K}_{\mathrm{R}} \boldsymbol{\Phi}_r^{\mathrm{T}} & \boldsymbol{\Phi}_z \mathbf{D}_{\mathrm{R}} \boldsymbol{\Phi}_z^{\mathrm{T}} \end{bmatrix} \begin{bmatrix} \widehat{\mathbf{p}}_{r,n} \\ \widehat{\mathbf{p}}_{z,n} \end{bmatrix} \tag{43}$$

where the matrix $\mathbf{D}_{\mathrm{R}} = \left(k^2 \mathbf{I} - \mathbf{K}_{\mathrm{R}}^2\right)^{-1}$.

For a given source, the displacement vector is computed via Eq. (43) and transformed into the frequency-space domain via Eq. (38). In the present work, the Green's functions are computed due to (i) a unit radial ring load at $r = R_{\mathrm{p}}$ ($n = 0$ and symmetric) and (ii) a unit vertical ring load at $r = R_{\mathrm{p}}$ ($n = 0$ and symmetric), as shown in Fig. 6. The explicit expressions for the latter in the framework of the TLM can be found in Kausel (1981).

Assembling together the Green's functions, the dynamic flexibility matrix $\widetilde{\mathbf{F}}_{\mathrm{s}}$ is obtained in the frequency-space domain, which relates the applied ring loads to the soil displacements as follows:

$$\begin{bmatrix} \widetilde{\mathbf{u}}_r \\ \widetilde{\mathbf{u}}_z \end{bmatrix} = \begin{bmatrix} \widetilde{\mathbf{F}}_{rr} & \widetilde{\mathbf{F}}_{rz} \\ \widetilde{\mathbf{F}}_{zr} & \widetilde{\mathbf{F}}_{zz} \end{bmatrix} \begin{bmatrix} \widetilde{\mathbf{p}}_{r,\mathrm{s}} \\ \widetilde{\mathbf{p}}_{z,\mathrm{s}} \end{bmatrix} \tag{44}$$

Similarly to the shell treatment in Section 2.1, in Eq. (44) the nonlinear pile–soil interaction forces will be accommodated in $\widetilde{\mathbf{p}}_{r,\mathrm{s}}$ and $\widetilde{\mathbf{p}}_{z,\mathrm{s}}$ as additional loading terms. The latter treatment is facilitated by the numerical solution method that will be presented in the ensuing.

2.3. Pile–soil compatibility conditions

The numerical method to be employed is based on the solution of the pile–soil system at discrete depths coinciding with the vertical mesh of pile and soil. Consider the pile at a certain embedment depth, where nodal rings and layer interfaces corresponding to the region of pile–soil contact are defined by the superscripts c and the remaining rings and interfaces (out-of-contact) are defined by the superscript nc. Therefore, vectors of quantities related to both pile and soil are partitioned into an in-contact and an out-of-contact part, e.g. $\mathbf{p}_{z,\mathrm{s}} = \begin{bmatrix} \left(\mathbf{p}_{z,\mathrm{s}}^{\mathrm{c}}\right)^{\mathrm{T}} & \left(\mathbf{p}_{z,\mathrm{s}}^{\mathrm{nc}}\right)^{\mathrm{T}} \end{bmatrix}^{\mathrm{T}}$ and $\mathbf{p}_{z,\mathrm{p}} = \begin{bmatrix} \left(\mathbf{p}_{z,\mathrm{p}}^{\mathrm{nc}}\right)^{\mathrm{T}} & \left(\mathbf{p}_{z,\mathrm{p}}^{\mathrm{c}}\right)^{\mathrm{T}} \end{bmatrix}^{\mathrm{T}}$. The latter partitioning into in-contact and out-of-contact quantities is employed in the following for both displacement and traction components. Evidently, the pile–soil interface is comprised by the lower part of the pile nodal rings (embedded) and the upper part of soil layer interfaces, irrespectively of the size of the contact region.

The pile and soil motions are described by Eq. (16) and Eq. (44), respectively, and the compatibility conditions that complete the mathematical formulation are:

(i) continuity of radial displacements at the pile–soil interface:

$$\mathbf{w}^{\mathrm{c}} = \mathbf{u}_r^{\mathrm{c}} \Big|_{r=R_{\mathrm{p}}} \tag{45}$$

(ii) compatibility of vertical tractions applied at the pile–soil interface and the pile tip:

$$\mathbf{p}_{z,\mathrm{s}}^{\mathrm{c}} = -\mathbf{p}_{z,\mathrm{p}}^{\mathrm{c}}, \quad p_{z,\mathrm{s}}^{(\mathrm{t})} = -p_{z,\mathrm{p}}^{(\mathrm{t})} \tag{46}$$

in which the superscript (t) denotes the tip related component. It is remarked that the load at the tip and the last entry of the load vector

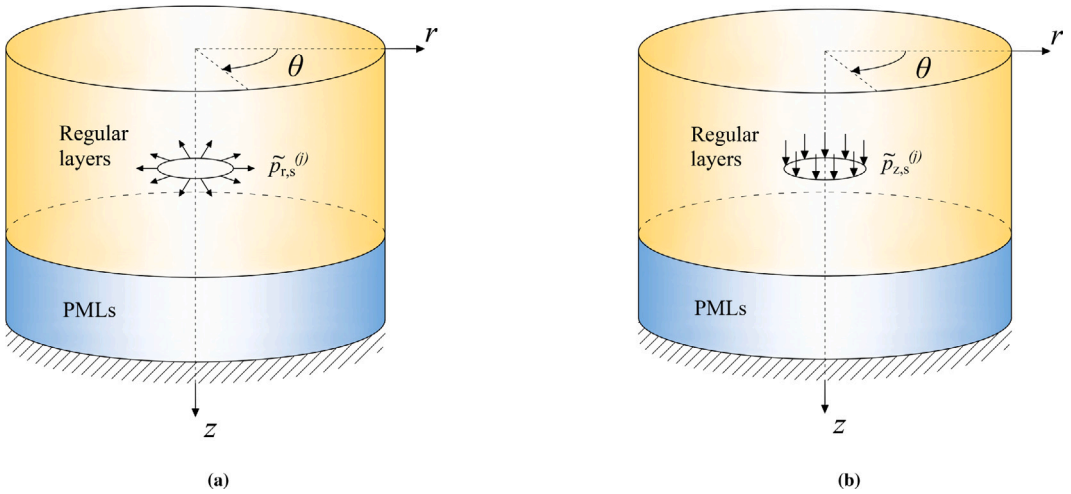

Fig. 6. Schematic of a (a) unit radial and (b) unit vertical ring source at elevation z_j.

at the shaft, correspond to the same nodal ring/layer interface, albeit they are split for computational purposes.

(iii) compatibility of radial tractions applied at pile and soil:

$$\mathbf{p}_{r,\mathrm{s}}^{\mathrm{c}} = -\mathbf{p}_{r,\mathrm{p}}^{\mathrm{c}} \tag{47}$$

The above conditions require the compatibility of tractions applied to both pile and soil along the shaft and at the tip, whereas continuity of displacements is retained only for the radial displacements. As regards the vertical motion, there is continuous pile sliding along the interface during installation, thus the vertical pile and soil velocities (and displacements) are different.

The frictional forces along the pile shaft are described according to a hereditary Coulomb friction law. Several numerical schemes are available for frictional contact problems; in the present work the hyperbolic tangent regularization is employed to retain computational efficiency and accuracy (Marques et al., 2016):

$$p_{z,\mathrm{s}}^{(i)} = -p_{z,\mathrm{p}}^{(i)} = f_{\mathrm{s,ult}}^{(i)} l^{(i)} \tanh\left(\frac{1}{v_{\mathrm{tol}}}\left(\frac{\partial u^{(i)}}{\partial t} - \frac{\partial u_z^{(i)}}{\partial t}\bigg|_{r=R_{\mathrm{p}}}\right)\right) \tag{48}$$

where v_{tol} is a velocity tolerance parameter, $l^{(i)}$ is the length of influence derived from the FE projection and $f_{\mathrm{s,ult}}^{(i)}$ defines the amplitude of the static (and kinetic) friction. It is remarked that Eq. (48) includes the friction forces resulting from both the inner and outer pile surfaces. A distinction between the two is beyond the scope of the present model.

In the present friction model, a memory mechanism is incorporated that leads to reduction of the friction amplitude under cyclic loading conditions. The latter effect is known to occur due to soil degradation and reduction of effective stresses in the immediate vicinity of the shaft (Holeyman, 2002). Moriyasu et al. (2018) performed field tests with different driving frequencies and found that the shaft degradation follows closely the number of loading cycles. We proceed to formulate such a hereditary law that incorporates that effect with the least number of parameters as follows:

$$f_{\mathrm{s,ult}}^{(i)} = f_{\mathrm{s},0}^{(i)}\left(\beta_\infty + (1-\beta_\infty)\mathrm{e}^{-c_N N_{\mathrm{cycl}}}\right) \tag{49}$$

where β_∞ is the ratio of the ultimately degraded friction amplitude to the initial one ($f_{\mathrm{s},0}^{(i)}$), c_N is a memory parameter that controls the rate of degradation and N_{cycl} is the number of loading cycles accumulated at the ith soil interface during driving. Therefore, the accumulation of loading cycles at a specific point in the soil, as the pile penetrates into the ground, leads to reduction of the friction force at this particular point.

The ring load at the pile tip includes a contribution of both shaft friction as well as tip reaction, due to the adopted discretization. For the tip reaction, the following local description is considered:

$$p_{z,\mathrm{s}}^{(\mathrm{t})} = -p_{z,\mathrm{p}}^{(\mathrm{t})} = \begin{cases} k_{\mathrm{t}}(u^{(\mathrm{t})} - u_{\mathrm{pl}}) + c_{\mathrm{t}}\dfrac{\partial u^{(\mathrm{t})}}{\partial t}, & |k_{\mathrm{t}}(u^{(\mathrm{t})} - u_{\mathrm{pl}})| < f_{\mathrm{t,ult}} h_{\mathrm{p}} \\ f_{\mathrm{t,ult}} h_{\mathrm{p}} \mathrm{sgn}\left(\dfrac{\partial u^{(\mathrm{t})}}{\partial t}\right) + c_{\mathrm{t}}\dfrac{\partial u^{(\mathrm{t})}}{\partial t}, & |k_{\mathrm{t}}(u^{(\mathrm{t})} - u_{\mathrm{pl}})| = f_{\mathrm{t,ult}} h_{\mathrm{p}} \end{cases} \tag{50}$$

where u_{pl} is the plastic tip displacement, $f_{\mathrm{t,ult}}$ is the plastic tip resistance and the distributed stiffness and damping coefficients are defined as k_{t} and c_{t}, respectively. The latter are extracted from the diagonal entry of the soil dynamic stiffness matrix $\widetilde{\mathbf{K}}_{\mathrm{s}}$ that corresponds to the pile tip; the matrix $\widetilde{\mathbf{K}}_{\mathrm{s}}$ is obtained via inversion of $\widetilde{\mathbf{F}}_{\mathrm{s}}$ given in Eq. (44). The present tip reaction model parallels that of a mechanical analogue comprised of a spring-slider in parallel with a viscous dashpot. However, in the present model the parameters k_{t} and c_{t} are derived from the exact dynamic stiffness of the layered soil medium and rely solely on standard soil properties, instead of being computed by approximate formulas and empirical parameters.

3. A solution to the coupled problem via the Harmonic Balance Method

In this problem, a time domain solution would be strictly prohibitive for engineering purposes, due to excessive computational cost. For that purpose, a novel solution scheme is proposed uniquely inspired by the physics of the installation process, based on the Harmonic Balance Method (HBM). The latter method has been successfully employed in various applications, such as buckling analysis of composite plates (Juhász and Szekrényes, 2015), vibrations of beams on non-linear and visco-elastic foundations (Bhattiprolu et al., 2016) and bladed discs in turbomachinery (Quaegebeur et al., 2022). However, its use in soil–structure interaction problems has not been realized as yet. In vibratory pile installation, the excitation induced by the vibrator is harmonic (or periodic), thus the HBM is appealing. However, the overall problem is not periodic as the pile penetration into the soil leads to an increase of the pile embedment and varying soil reaction along the shaft and at the tip. Therefore, we pursue a solution based on multiple sequential HB analyses for different pile positions, that once assembled together can provide the total solution. The present approach is structured as follows:

(i) First, we define a compatible vertical mesh for the pile (SAFE) and soil (TLM), e.g. uniform mesh of identical size.

(ii) For each compatible position, i.e. elevations at which pile nodal rings and soil layer interfaces coincide, a solution is sought via the

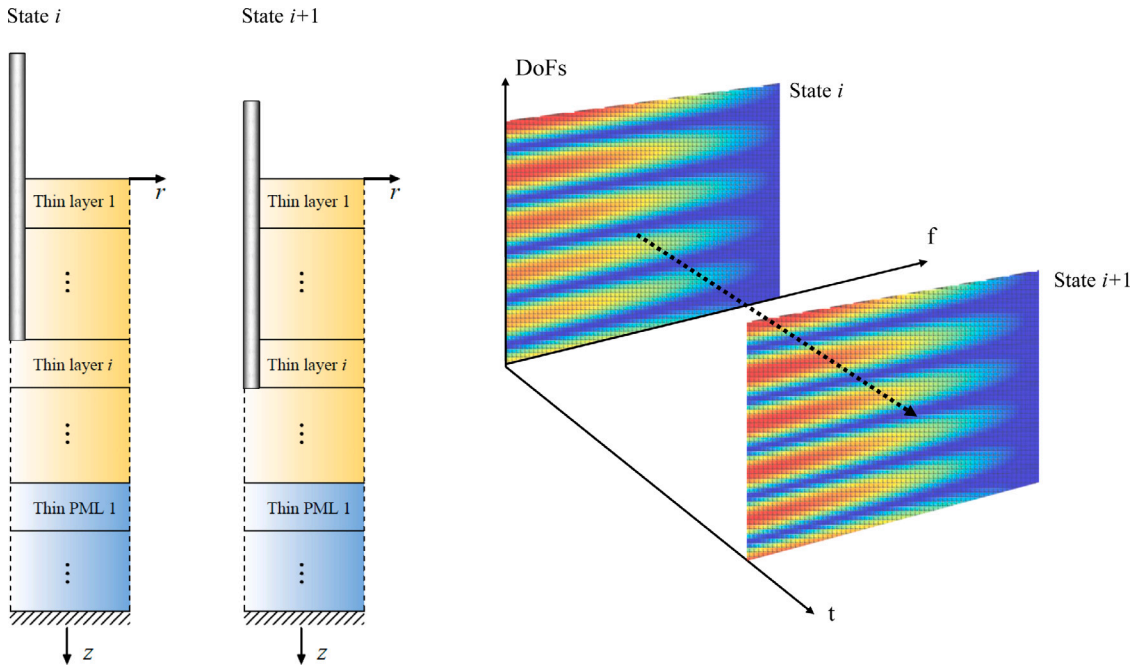

Fig. 7. Schematic of the sequential HB approach for two pile positions i and $i+1$, accompanied by the linear interpolation of the HB coefficients in the frequency-time plane.

HBM. This solution is valid for a time interval significantly larger than the HB fundamental period, as the pile position and overall response varies in a much slower rate than the driving frequency (different time scales). Therefore, the HB coefficients for each pile position along the mesh can be found in a sequential manner.

(iii) The HB coefficients are considered to vary linearly in the transition from each position to the subsequent one, given that the adjacent positions are close enough to allow for such an approximation.

(iv) The solutions from each HB analysis are assembled into the total solution, leading effectively to amplitude modulation of the involved harmonics and thus an overall quasi-periodic system response.

A visual representation of the process described is also shown in Fig. 7. Two adjacent positions are denoted by states i and $i+1$ and linear interpolation of the resulting HB coefficients takes place to transition from state i to state $i+1$. It is noted that by DoFs we consider all the quantities that are approximated by the HBM.

We proceed to define our solution ansatz according to the HBM. For the pile modal coordinates the following ansatz is considered:

$$q^{\mathrm{s}}_{0,m} = \begin{cases} c_{0,0}t + \sum_{j=1}^{N_{\mathrm{h}}} \left(c_{0,j} \cos(j\Omega t) + s_{0,j} \sin(j\Omega t) \right), & m = 0 \\ c_{m,0} + \sum_{j=1}^{N_{\mathrm{h}}} \left(c_{m,j} \cos(j\Omega t) + s_{m,j} \sin(j\Omega t) \right), & m > 0 \end{cases} \tag{51}$$

where $\mathbf{c}_m = \begin{bmatrix} c_{m,0} & c_{m,1} & \cdots \end{bmatrix}^{\mathrm{T}}$ and $\mathbf{s}_m = \begin{bmatrix} s_{m,1} & s_{m,2} & \cdots \end{bmatrix}^{\mathrm{T}}$ denote the vectors encapsulating the Fourier coefficients of the mth mode related to the cosine and sine terms, respectively. As can be seen, the ansatz that corresponds to the rigid body mode ($m = 0$) is periodic in velocity, such that linear pile progression into the soil with time can be addressed (Tsetas et al., 2022a).

To obtain the soil response, it is chosen to approximate the non-linear reaction forces at the soil–pile interface and at the tip as Fourier series. Furthermore, to reduce the dimensionality of the friction forces along the pile–soil interface, a matrix decomposition of the following form is applied:

$$\mathbf{p}^{\mathrm{c}}_{\mathrm{s},z} = \boldsymbol{\Psi} \left(\boldsymbol{\alpha}_0 + \sum_{j=1}^{N_{\mathrm{h}}} \left(\boldsymbol{\alpha}_j \cos(j\Omega t) + \boldsymbol{\beta}_j \sin(j\Omega t) \right) \right) \tag{52}$$

in which $\boldsymbol{\alpha}_j$ and $\boldsymbol{\beta}_j$ are the vectors of the Fourier coefficients related to the jth cosine and sine terms and the matrix $\boldsymbol{\Psi}$ encapsulates the basis vectors employed to approximate the spatial distribution of the interface forces. In particular, these basis vectors are obtained by projection of the respective function class to the vertical FE mesh; a multitude of functions is suitable for that purpose, e.g. Lagrange polynomials, Fourier-based shape functions and B-splines (Gravenkamp et al., 2021). As follows from the HBM, the tip reaction is also assumed to be periodic:

$$p^{(\mathrm{t})}_{\mathrm{s},z} = \alpha_{\mathrm{t},0} + \sum_{j=1}^{N_{\mathrm{h}}} \left(\alpha_{\mathrm{t},j} \cos(j\Omega t) + \beta_{\mathrm{t},j} \sin(j\Omega t) \right) \tag{53}$$

where $\boldsymbol{\alpha}_{\mathrm{t}} = \begin{bmatrix} \alpha_{\mathrm{t},0} & \alpha_{\mathrm{t},1} & \cdots \end{bmatrix}^{\mathrm{T}}$ and $\boldsymbol{\beta}_{\mathrm{t}} = \begin{bmatrix} \beta_{\mathrm{t},1} & \beta_{\mathrm{t},2} & \cdots \end{bmatrix}^{\mathrm{T}}$ denote the vectors encapsulating the Fourier coefficients of the tip reaction related to the cosine and sine terms, respectively.

In all the above equations, the involved quantities are in the space–time domain. Based on the premise of periodic response, the inverse Fourier transform of the soil displacements and loads from frequency to time domain is analytically tractable and will not be elaborated. By substituting the assumed solutions into the dynamic equilibria of pile and soil and the compatibility conditions, it can be shown that the following residuals are required to vanish:

$$\begin{aligned} \mathbf{r}_{\mathrm{c}} &= \boldsymbol{\Psi}^{\mathrm{T}} \left(\mathbf{p}^{\mathrm{c}}_{\mathrm{s},z} + \mathbf{p}^{\mathrm{c}}_{\mathrm{p},z} \right), \quad r_{\mathrm{t}} = p^{(\mathrm{t})}_{\mathrm{s},z} + p^{(\mathrm{t})}_{\mathrm{p},z}, \\ \mathbf{r}_q &= \left(\boldsymbol{\Phi}^{\mathrm{s}}_{\mathrm{p},0} \right)^{\mathrm{T}} \left(\mathbf{I}^{\mathrm{s}}_0 \boldsymbol{\Phi}^{\mathrm{s}}_{\mathrm{p},0} \frac{\mathrm{d}^2 \mathbf{q}^{\mathrm{s}}_0}{\mathrm{d}t^2} + \mathbf{L}^{\mathrm{s}}_0 \boldsymbol{\Phi}^{\mathrm{s}}_{\mathrm{p},0} \mathbf{q}^{\mathrm{s}}_0 - \mathbf{p}^{\mathrm{s}}_{\mathrm{p},0} \right) \end{aligned} \tag{54}$$

which can be arranged in the following residual vector:

$$\mathbf{r} = \begin{bmatrix} \mathbf{r}_{\mathrm{c}} \\ r_{\mathrm{t}} \\ \mathbf{r}_q \end{bmatrix} \tag{55}$$

Following the HBM, we require that the Fourier coefficients of the residual vector $\mathbf{r}$ vanish up to the truncation limit and are obtained via a Fourier–Galerkin projection as follows:

$$\mathbf{R}_{\mathrm{F}} = \frac{1}{T}\int_0^T \mathbf{r}\mathbf{h}\,\mathrm{d}t, \quad \mathbf{h} = \left[1\ \cos(\Omega t)\ \cdots\ \cos(N_{\mathrm{h}}\Omega t)\ \sin(\Omega t)\ \cdots\ \sin(N_{\mathrm{h}}\Omega t)\right] \tag{56}$$

where $\mathbf{R}_{\mathrm{F}}$ is a matrix that encapsulates the Fourier coefficients of the residuals and T is the period corresponding to the fundamental frequency, i.e. the driving frequency Ω. It is noted that the non-linear reaction forces in the present problem cannot be analytically expanded in terms of the assumed Fourier coefficients, thus the Alternating Frequency-Time (AFT) HBM is applied (Laxalde and Thouverez, 2009; Fontanela et al., 2019). The latter is based on the evaluation of the non-linear forcing terms in the time domain and the subsequent application of the Discrete Fourier Transform (DFT) via the Fast Fourier Transform (FFT) algorithm. The AFT-HBM entails an iterative process that in our solution approach is posed as a vector optimization problem and customarily is solved by the Newton–Raphson or similar algorithms (Krack and Gross, 2019; Laxalde and Thouverez, 2009; Krack et al., 2013). In our solution scheme, the Powell's hybrid method is found to be superior both in terms of accuracy and computational performance and is employed in the ensuing analyses (Powell, 1970).

Briefly, the overall process can be summarized as follows:

(i) a periodic ansatz is considered for the pile modal coordinates (Eq. (51)) and the vertical tractions (Eqs. (52) and (53)), thus the pile and soil displacement fields can be obtained via Eqs. (17) and (44), respectively. It is remarked that the radial soil displacements are directly obtained via Eq. (45).

(ii) a residual is formed by the assumed tractions and the tractions resulting from the pile–soil relative motion according to Coulomb's friction (Eq. (48)). Similarly, the residual of the SAFE equations of motion in the modal domain is formed.

(iii) the Fourier coefficients of the preceding residuals are required to vanish – implying vanishing of the residuals – according to the HBM. The vectors of Fourier coefficients ($\mathbf{c}_m$, $\mathbf{s}_m$, $\boldsymbol{\alpha}_j$, $\boldsymbol{\beta}_j$, $\boldsymbol{\alpha}_{\mathrm{t}}$, $\boldsymbol{\beta}_{\mathrm{t}}$) obtained from the vector optimization problem and leading to $\mathbf{R}_{\mathrm{F}} = \mathbf{0}$ provide the final solution to the problem.

Conclusively, the described procedure corresponds to the solution of the system at a single embedment depth. For each subsequent depth, it follows that the involved vector and matrix quantities need to updated in accordance with Fig. 2.

4. Numerical validation of model components

The numerical components that have been introduced in this paper are first benchmarked against established numerical schemes. In particular, the SAFE shell model, the Green's functions obtained via the TLM+PMLs and the sequential HB solution method are validated in the ensuing.

4.1. Validation of the SAFE cylindrical shell model

A SAFE model for cylindrical shells has been presented in Section 2.1. In our problem, the symmetric configuration for $n = 0$ is only used, so we proceed to validate the developed SAFE model for $n = 0$. For that purpose, the SAFE approach is compared against an FE model developed in COMSOL Multiphysics® software (COMSOL AB, 2022). A free–free cylindrical shell is considered, which is modelled in COMSOL by means of MITC shell elements (Chapelle and Bathe, 2010). The pile properties are presented in Table 1. In Fig. 8, the natural frequencies of the first 30 modes for $n = 0$ are found by the SAFE shell model and compared with those obtained from COMSOL. Evidently, the agreement is such that the two sets are virtually indistinguishable.

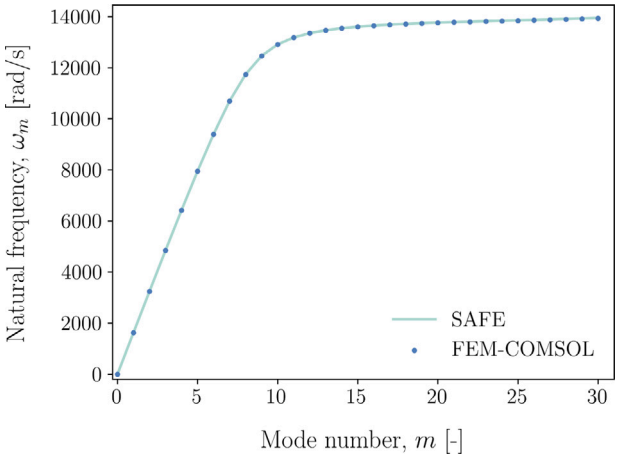

Fig. 8. Comparison of natural frequencies obtained from the SAFE model and the FE (COMSOL) model for $n = 0$.

Table 1
Pile parameters for the validation of the SAFE shell model.

ρ_{p} [kg/m^3]	E_{p} [Pa]	ν_{p} [-]	L_{p} [m]	R_{p} [m]	h_{p} [m]
7850	$210{\cdot}10^9$	0.3	10	0.373	0.0159

Table 2
Soil parameters for the validation case of the Green's functions.

	ρ_{s} [kg/m^3]	G_{s} [MPa]	ν_s [-]	ξ_{s} [-]
Upper soil layer	2000	20	0.3	0.025
Bottom half-space	1800	23	0.499	0.025

4.2. Validation of the Green's functions via the TLM+PMLs

In the present work, the Green's functions of a linear elastic layered half-space are obtained via the TLM coupled with PMLs (TLM+PMLs). For validation purposes, the TLM+PMLs results are compared with those of an FE model developed in COMSOL.

The case study is based on a two-layer soil profile as described in Table 2. Hysteretic soil damping is considered in the form of complex-valued Lamé constants, where the damping ratio ξ_{s} is taken identical for both dilatational and distortional waves. A harmonic ring source (vertical or radial) with frequency $f = 23$ Hz is applied at $z = 4$ m and $r = 0.4$ m, while the Green's functions are evaluated along the vertical axis and at the source radius. The upper layer is unsaturated with a thickness $H_{\mathrm{EL},1} = 5$ m and underlain by a water-saturated half-space. In the TLM+PMLs, the half-space is substituted by a linear elastic layer with thickness $H_{\mathrm{EL},2} = 5$ m and a PML domain with thickness $H_{\mathrm{PML}} = 5$ m. For the half-space approximation in the COMSOL model, a linear elastic layer with large depth is used ($H_{\mathrm{EL},2} = 25$ m) and supported below by a horizontal low-reflecting boundary. Similarly, the radial extent of the FE model is finite with a domain radius of 50 m and bounded by a cylindrical low-reflecting boundary. In the TLM+PMLs, such an approach is altogether avoided, due to analytical solutions employed in the radial direction that satisfy the radiation condition at infinity. In Fig. 9, the Green's functions are compared for the cases of radial and vertical ring loads. As can be seen, the results agreement between the TLM+PMLs and the FE model is remarkable for both load

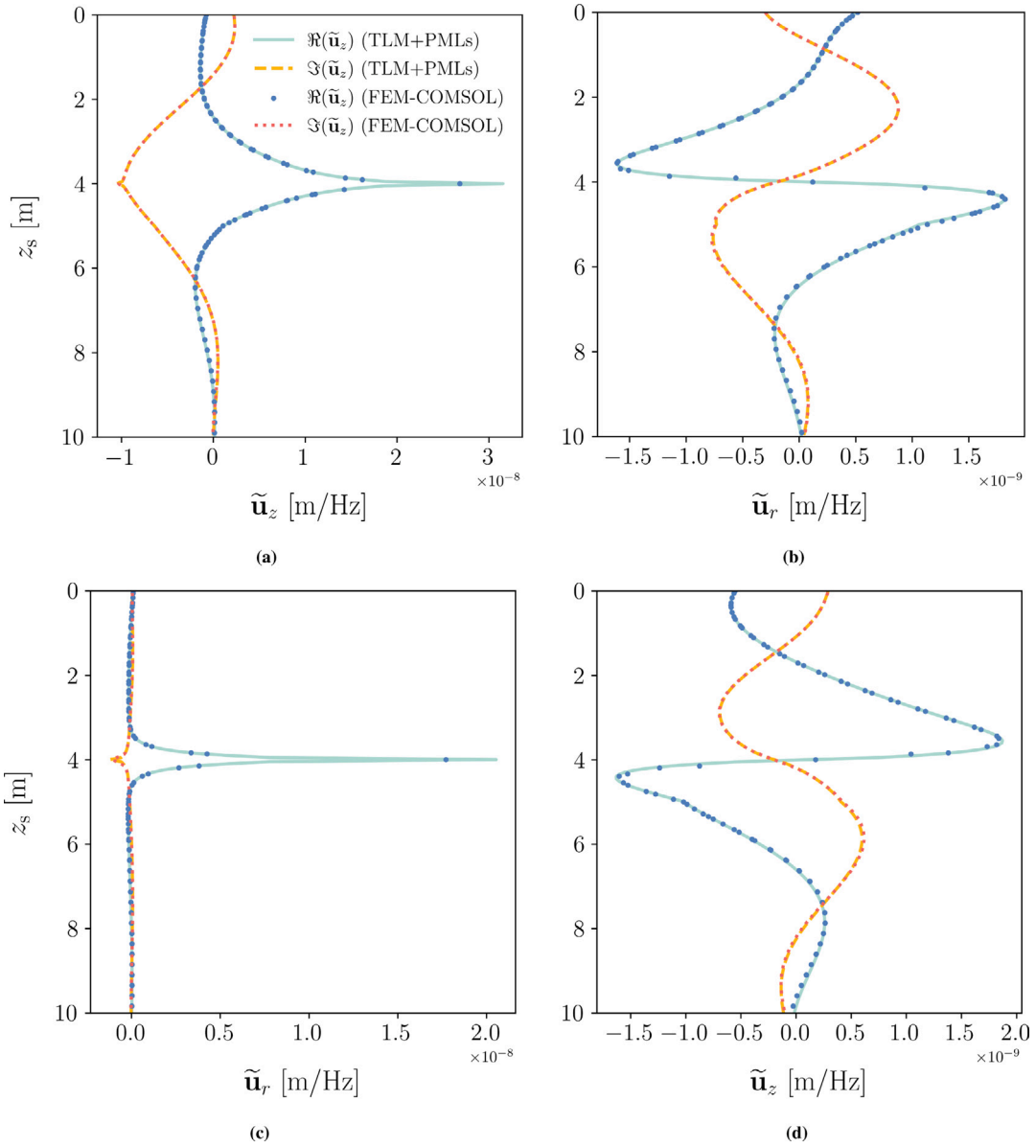

Fig. 9. Comparison of Green's functions obtained via the TLM+PMLs and the FE (COMSOL) model for (a,b) a unit vertical ring load and (c,d) a unit radial ring load.

cases, with sole discrepancy in Figs. 9(a) and 9(c) the source-receiver concurrence which is expected due to singularity.

4.3. Validation of a linear pile–soil model via coupling of the SAFE method and the TLM+PMLs

As a final validation of the pile and soil components, the linear dynamic response of a pile embedded in a homogeneous half-space is considered. Specifically, the pile properties are given in Table 1 and the embedment length is equal to half of the pile length ($L_{\text{emb}} = 0.5L_{\text{p}}$). Furthermore, the soil domain is described as a linear elastic soil half-space with properties identical to the ones of the upper layer in Table 2. The pile–soil coupling is realized by combining the dynamic stiffness matrices of pile and soil via substructuring (Géradin and Rixen, 2014). For the pile, the dynamic stiffness matrix is readily derived by applying the Fourier transform to Eq. (14) (and division by $2\pi R_{\text{p}}$), and for the soil by inverting the dynamic flexibility matrix (Eq. (44)) via spectral decomposition. The compatibility conditions of displacements and tractions (both vertical and radial) are invoked and the full pile–soil system is partitioned into pile DoFs, soil DoFs and pile–soil DoFs along the interface (shaft and tip). Without further details, the resulting axial ($\widetilde{\mathbf{u}}$) and radial ($\widetilde{\mathbf{w}}$) pile responses are shown in Fig. 10 for a unit vertical ring load applied at the pile top with frequency $f = 23$ Hz. As can be seen the agreement between the SAFE+TLM+PMLs approach and the FE model is remarkable and demonstrates the capability of the present framework to address also the problem of linear pile–soil interaction. In the ensuing, the numerical method that facilitates the coupling in the non-linear problem is benchmarked, namely the sequential HBM.

4.4. Validation of the sequential HBM

In Section 3, a new solution scheme based on the HBM has been presented for the problem at hand. To focus on the validation of the proposed sequential HB solution scheme, we formulate a corresponding 1-D problem (Tsetas et al., 2022b). Specifically, two rods in frictional contact are considered, where the first rod is free to slide along the second. Modal decomposition is applied to rod 1 and rod 2 is described via Green's functions in the frequency domain, as in the solution approach adopted in the pile–soil problem. The advantage of this benchmark

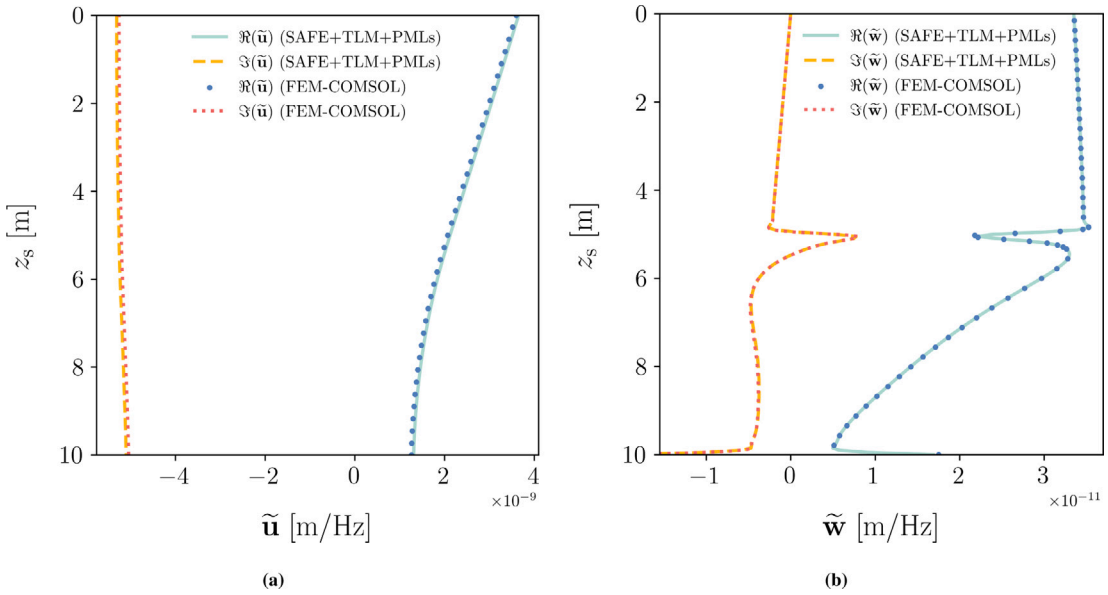

Fig. 10. Comparison of (a) axial ($\widetilde{\mathbf{u}}$) and (b) radial ($\widetilde{\mathbf{w}}$) responses of an embedded pile obtained via the coupled SAFE+TLM+PMLs model and the FE (COMSOL) model for a unit vertical ring load applied at the pile top.

problem is that it lends itself to direct solution in the time domain via numerical integration. Specifically, an explicit Runge–Kutta method (RK45) is employed (Dormand and Prince, 1980). In Appendix B the problem of the two rods in frictional contact is outlined and more details can be found in Tsetas et al. (2022b).

The properties of the two rods are identical to the ones given in Table 1 and the contact region is equal to 50% of their length. A harmonic excitation with amplitude $P_1 = 100$ kN and frequency $\Omega_1 = 157.08$ rad/s is applied at the top of rod 1, along with a static force $P_0 = 10$ kN. The contact interface is described by Coulomb friction with amplitude $f_c = 8.379$ kN/m, which is constant along the longitudinal axis. In Fig. 11, the displacement at the top of rod 1 is shown. The dashed red line corresponds to the first HB solution found at the initial position of rod 1 and is used to indicate the initial (and maximum) penetration rate. As rod 1 progresses and the contact length increases, the penetration rate reduces due to the increase of the total friction force. As can be seen, the proposed sequential HBM scheme captures remarkably the overall penetration process.

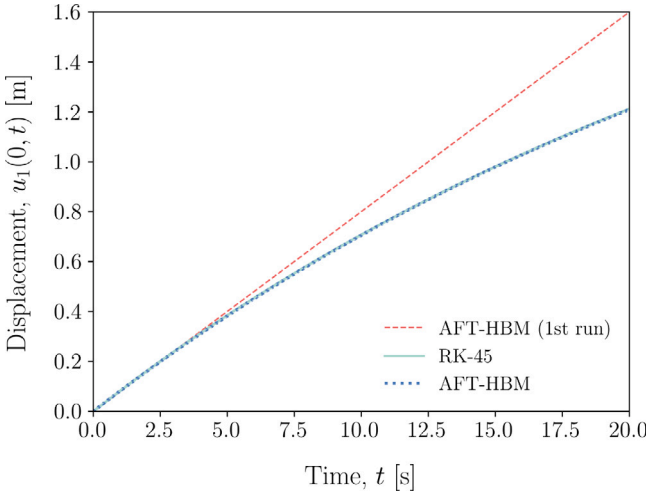

Fig. 11. Comparison of displacement at top of rod 1 obtained via numerical integration (RK-45) and the sequential AFT-HBM.

5. Comparison of numerical and experimental results

The presented numerical model is used to study a vibratory-driven pile from the 'Gentle Driving of Piles' (GDP) experimental campaign (Tsetas et al., 2023; Kementzetzidis et al., 2023). First, input data from *in-situ* tests are used to characterize the relevant model parameters. Subsequently, model predictions are compared with field data and the effect of the driving frequency is studied theoretically.

5.1. Input data

In the GDP campaign different installation methods (impact, axial vibratory and GDP) were tested and the pile considered herein is the only one installed via vibro-driving (VH). An aerial view of the test site is shown in Fig. 12. The driven pile properties are identical to those described in Table 1 and the specifications of the vibratory device are given in Table 3. For both pile and soil, hysteretic damping is considered with ratios $\xi_p = 0.001$ and $\xi_s = 0.025$ (for both P- and S-waves), respectively. In the installation tests, for the upper 3 m the pile was laterally restrained to eliminate any inclination and controlled by a crane, thus the interval from 3 m to 8 m is considered in this study.

The dynamic excitation at the pile top is introduced in the model based on strain measurements via fibre Bragg grating (FBG) sensors; the FBG sensors were located 1.62 m from the pile top. In our solution approach via the HBM, the dynamic excitation is considered nearly stationary, i.e. periodic for time intervals significantly larger than the fundamental period during which we apply the HBM. The latter has been found to hold for both vibratory methods (VH and GDP) in the GDP field tests (Gómez et al., 2023; Tsetas et al., 2023). Furthermore, a time–frequency analysis of the top axial strain ($\epsilon_{zz,p}$) by means of a discrete short-time Fourier transform (STFT) is also performed to support that finding. As can be seen in Fig. 13, the frequency content and the associated amplitudes remain fairly constant during installation, indicating a quasi-periodic excitation due to amplitude modulation of the involved harmonics.

For the characterization of the soil properties, Seismic Cone Penetration Tests with pore water pressure measurements (SCPTu) were performed (see Fig. 14) and the depth of the water table was found

Fig. 12. The test site of the GDP field campaign.

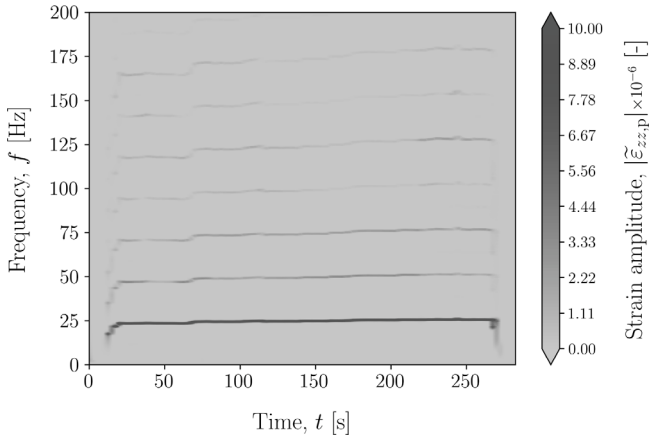

Fig. 13. Amplitude of the axial strain ($|\tilde{\varepsilon}_{zz,\mathrm{p}}|$) STFT for the VH pile.

Table 3
Technical specifications of the vibro-hammer CV-25.

Mass [kg]	Eccentric moment [kgm]	Rotational speed [rpm]	Operational power [kW]
4100	25	1800	204

at 4.5 m. From the SCPTu measurements, the basic soil properties that characterize the linear elastic layered medium can be obtained. Therefore, the Green's functions can be directly computed, as well as the values k_{t} and c_{t} that follow from the dynamic stiffness matrix. In general, ultimate shaft resistance (friction amplitude) as well as ultimate tip resistance have been found to correlate strongly with the cone tip resistance q_c measured during CPTs (Randolph et al., 1994; Schneider et al., 2008). The relevant studies were focused on static axial pile capacity and recent field tests by Moriyasu et al. (2018) investigated such correlations also in the case of vibro-driving of pipe piles. Based on the latter tests, an initial friction amplitude of $f_{\mathrm{s},0}^{(i)} = 0.012 q_c(z_i)$ is adopted in our analysis. Regarding the ratio of ultimately degraded to initial shaft resistance, a value of $\beta_\infty = 0.2$ is selected for the sandy soil considered (Jonker, 1987; Bielefeld et al., 2020). In the latter studies the ultimately degraded value is typically reached at approximately 10 000 loading cycles, while a range from approximately 7000 to 15 000 cycles was observed by Moriyasu et al. (2018). For the memory mechanism of our friction model, this range of loading cycles corresponds to c_N values between 0.0003 and 0.0005. For the tip reaction during vibratory driving, field observations are scarce, so we investigate a range of $f_{\mathrm{t,ult}}$ values. As will be shown in the ensuing, this uncertainty has insignificant effect on the pile drivability. Notwithstanding the previous, dynamic CPTs (e.g. VCPT (Al-Sammarraie et al., 2022)) that allow to control the vibration amplitude and the driving frequency of the cone penetrometer may be more suitable for parameter calibration in vibratory driving.

5.2. Measurements and model predictions

In Fig. 15, the pile penetration is shown, as measured by the potentiometer transducer (PM) and the driving logging (DL) system. The former measurement has a high sampling rate ($f = 1000$ Hz) and is considered more reliable than the latter, which is a sparse measurement (recorded per 25 cm of penetration). As can be seen, the predictions of the model provide fairly similar penetration trends and form an upper and lower bound (of soil reaction), respectively. The best prediction was found for $c_N = 0.0004$ for the overall duration of installation (in least squares sense). This result is promising for the predictive potential of our model, considering the small number of non-standard parameters that need to be calibrated and its robust theoretical formulation. In Table 4, a summary of the parameters that characterize the shaft and tip reactions is given. It is remarked that four out of the six parameters can be characterized directly from (S)CPTs, while the degradation rate (c_N) and the ultimate-to-initial friction ratio (β_∞) are non-standard parameters and intrinsically related to the soil material. The calibration

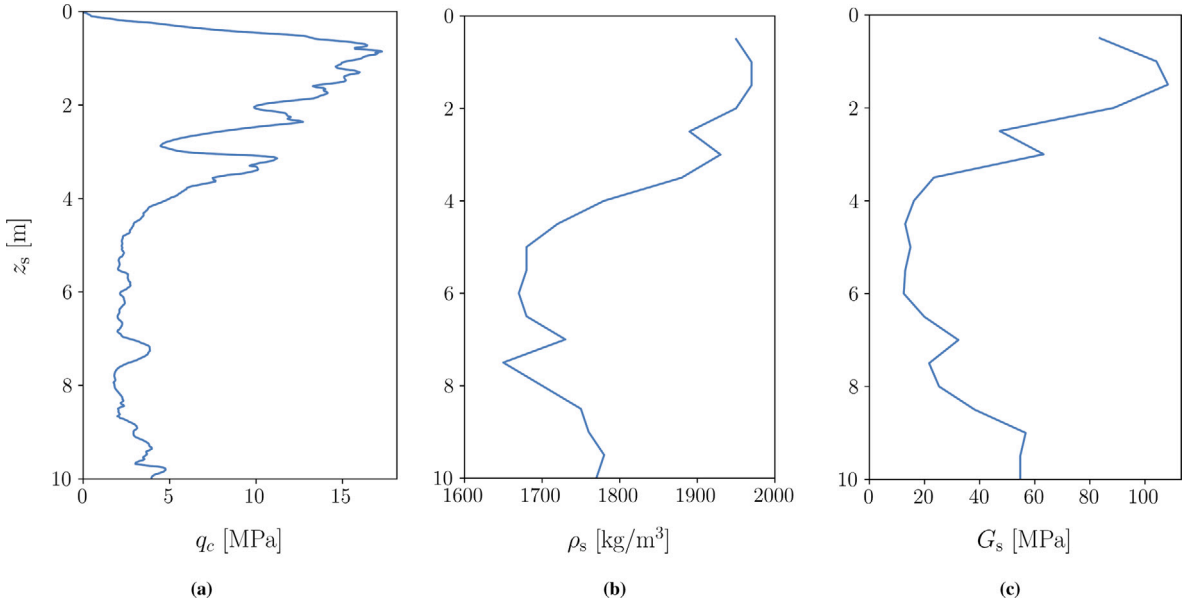

Fig. 14. Profiles of (a) cone tip resistance (q_c), (b) mass density (ρ_s), and (c) shear modulus (G_s) obtained from the SCPTu tests.

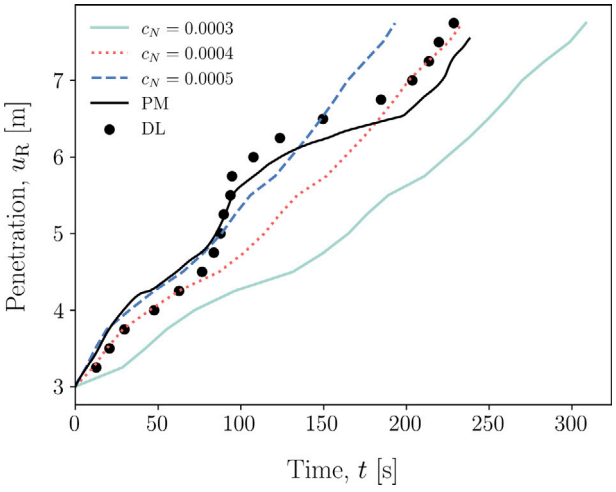

Fig. 15. Comparison of vibratory installation model predictions with field data as recorded by a potentiometer (PM) and the vibratory device logging system (DL).

process of the full parameter set is expected to improve with the inflow of additional field data in order to facilitate the use of the present model in engineering practice.

For the analyses shown in Fig. 15, $f_{t,ult} = 0.5q_c(z_t)$ was considered in the tip reaction model, due to its fair comparison with the FBG-measured reaction 0.5 m from the pile tip as shown in Fig. 16(a). We proceed to showcase that the tip reaction uncertainty is of minor importance for the penetration process of the studied pile. In Fig. 16(b), the penetration for different analyses is shown, where a range of $f_{t,ult}$ from $0.3q_c(z_t)$ to $0.7q_c(z_t)$ has been considered. Based on the two extrema ($f_{t,ult} = 0.3q_c(z_t)$ and $f_{t,ult} = 0.7q_c(z_t)$), an increase of the plastic tip resistance $f_{t,ult}$ by 133.3% led to a minor increase of 12.8% in the total installation time. Therefore, for the present pile the effect of the tip reaction on the installation rate is secondary and the pile–soil friction at the shaft provides the main resistance to driving. To elaborate further, the comparison of the tip and the total shaft reactions (as line loads) is depicted in Fig. 17(a), where the total shaft reaction comprises the major component. In Fig. 17(b), the total shaft and tip reactions are given as fractions of the total soil reaction $\left(p_{z,s}^{(t)} + \sum_i p_{z,s}^{(i)}\right)$, whereas the average of the two ratios during installation are approximately 77% and 23% for the shaft and tip components, respectively. This observation is expected to be even more prominent in the installation of offshore monopiles given the significantly larger embedment depth. For that purpose, field campaigns that include in their scope the identification of the memory mechanism that leads to soil–pile friction reduction are considered of major importance for better understanding the vibratory installation process.

It is interesting to note the relatively small variation of the total shaft reaction during installation in Fig. 17(a), which results from the cyclic memory mechanism. To better visualize the latter effect, Fig. 18 presents the distribution of the friction amplitude $f_{s,ult}^{(i)}$ along depth z for different instances during driving, i.e. every 0.5 m of pile penetration. The gradual reduction of friction amplitude with number of cycles and the "saturation" of the degradation effect in the shallow soil layers are both clearly visible. Naturally, the proposed cyclic memory mechanism is an effective one and at this stage it does not assume dependence on variables that may be of importance, e.g. driving frequency, loading cycle amplitude and surface roughness. Both experimental and numerical studies are required to better understand the physical mechanisms at hand and develop a formulation that incorporates such additional dependencies with a view to installation modelling.

5.3. Effect of driving frequency on penetration rate

An interesting aspect of vibratory driving is the effect of the driving frequency on the penetration rate. We proceed to analyse the penetration of the VH pile for a range of driving frequencies without altering any other parameter (e.g. excitation amplitude). In Fig. 19, the average penetration rates for all driving frequencies and degradation rate values c_N are shown. The general trend indicates that the average penetration rate is a monotonic function of frequency for the examined range, i.e. from 16 Hz to 60 Hz. This observation persists for all three c_N values considered and a plateau region becomes apparent above 45 Hz. A similar trend has also been reported by Xiao and Ge (2022), based on numerical analyses. Field experiments that will investigate the effect of driving frequency are necessary to test the validity of the trend

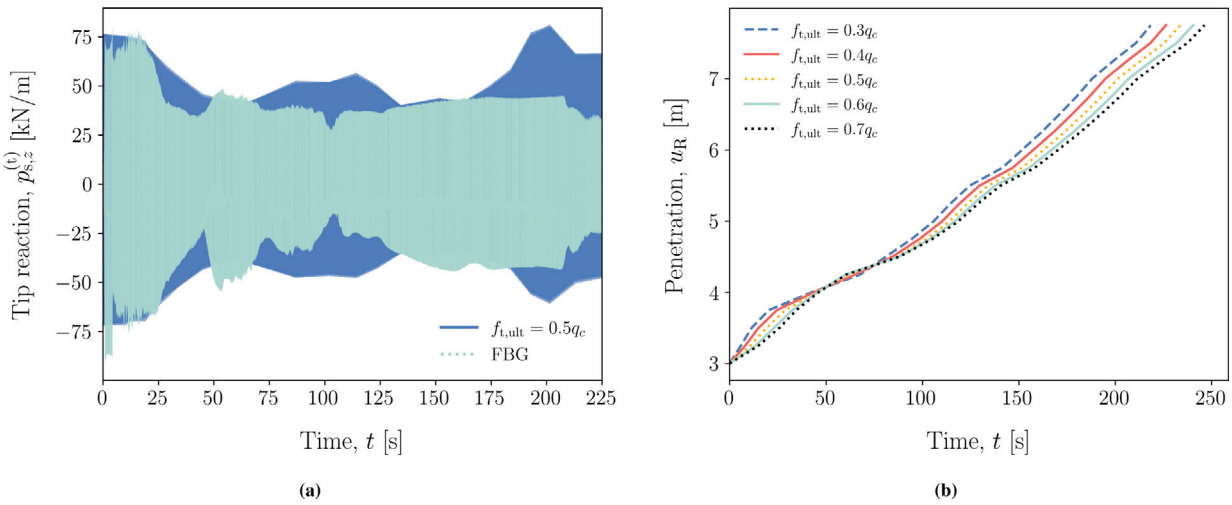

Fig. 16. (a) Comparison of tip reaction $p_{s,z}^{(t)}$ from the vibratory installation model ($f_{t,ult} = 0.5q_c(z_t)$) with the FBG-based axial force resultant close to the pile tip. (b) Comparison of penetration model predictions for different ultimate tip resistance $f_{t,ult}$ values.

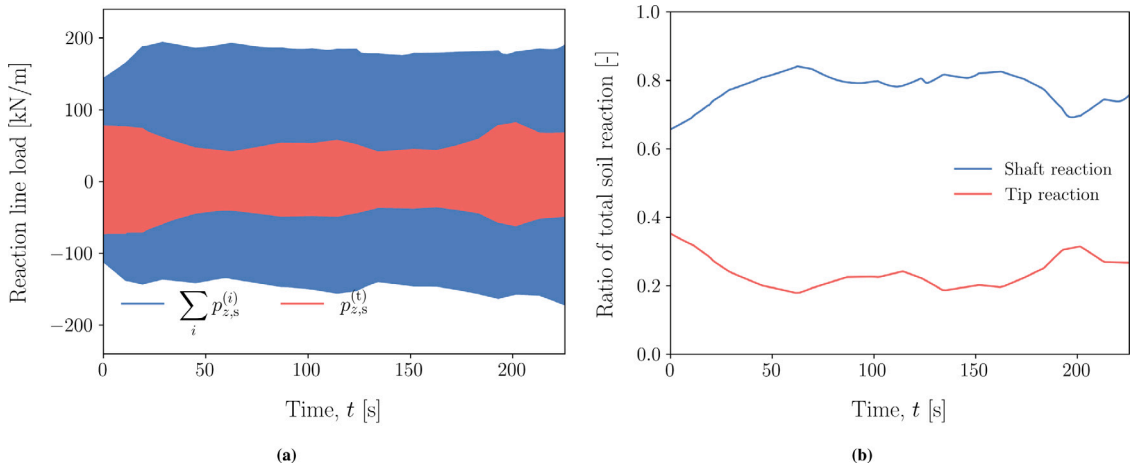

Fig. 17. (a) Total shaft and tip reactions during driving and (b) ratios of total shaft and tip reactions to total soil reaction during driving.

Table 4
Summary of soil reaction parameters for the vibratory driving model.

Shaft reaction			Tip reaction		
$f_{s,0}^{(i)}$ [Pa]	β_∞ [-]	c_N [-]	$f_{t,ult}$ [Pa]	k_t [Pa]	c_t [Pa·s]
$0.012q_c(z_i)$	0.2	0.0004	$0.5q_c(z_t)$	extracted from $\widetilde{\mathbf{K}}_s$	extracted from $\widetilde{\mathbf{K}}_s$

presented in Fig. 19, as well as the effect of driving frequency on the post-installation performance.

5.4. Computational aspects of the model

Conclusively, the present model has been developed to improve the existing medium-fidelity approaches. Therefore, some additional details regarding its computational performance are required. For both pile and soil a vertical mesh of size $h = 0.05$ m was considered, while 5 trial functions (i.e. modes) were adequate to obtain an accurate pile response. As regards the velocity tolerance v_{tol} of the frictional interface, all response quantities are found unaffected for v_{tol} below 1% of the relative velocity extrema occurring during a cycle of motion. Given the HB-based scheme, the relative velocity at the pile–soil interface is known prior to the optimization process, thus the threshold is adaptive and constantly less than 1% of the relative velocity extrema. In the HB analyses, terms up to the 15th super-harmonic were retained (31 terms in total) in each Fourier series. A parametric study of 54 numerical analyses for the VH pile was performed in a computer desktop with a 10-core 3.3 GHz processor. A parallel implementation of the described task had a run time of 3 h, leading to a remarkable CPU time of 3∼4 min per analysis (for 5 m of pile penetration). Therefore, the present modelling framework can be readily employed in large parametric and uncertainty quantification studies.

6. Conclusions

In this paper, a computationally efficient model for vibratory pile installation has been presented, that aims to bridge the gap between medium- and high-fidelity approaches. The pile is described by a thin shell theory and the soil is modelled as a linear elastic layered half-space. In particular, a SAFE model is used for the thin cylindrical shell and the Green's functions in the frequency-space domain are computed for the layered soil medium via the TLM coupled with PMLs. The pile–soil interaction is described by a history-dependent frictional

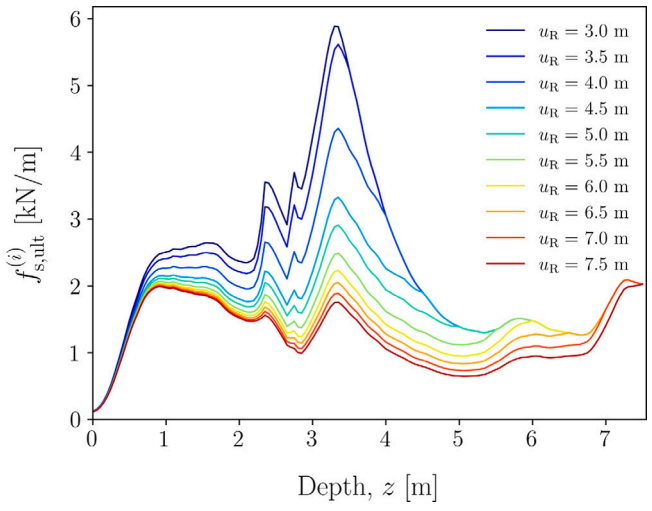

Fig. 18. Friction amplitude distribution along soil depth z for different penetration depths (per 0.5 m), showcasing the memory effect on shaft friction reduction.

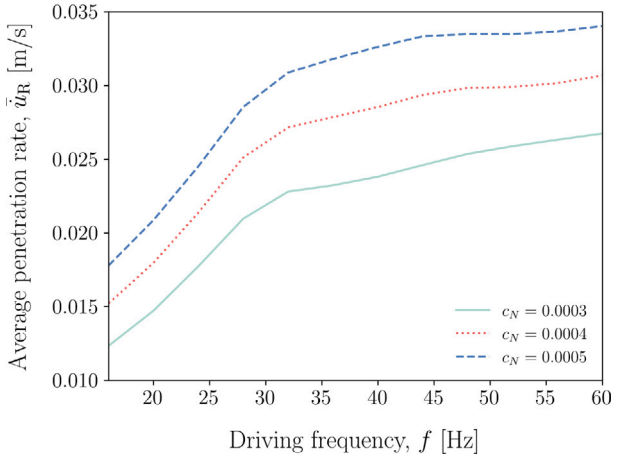

Fig. 19. Comparison of average penetration rates for different driving frequencies, based on model predictions.

interface, based on loading cycles accumulation and a visco-elasto-plastic tip reaction model, both characterized by SCPT measurements. For the solution of the coupled problem, a sequential HBM has been developed, that was motivated by the quasi-periodic character of the response. The latter approach comprises a remarkably efficient scheme for this problem and a potential candidate for a wider class of systems with quasi-periodic response due to slow amplitude modulation of the involved harmonics. The present modelling framework was employed to study the case of a vibro-driven pile from the GDP field campaign. Conclusively, the numerical results were compared with field data and the major points are listed as follows:

– vibratory pile installation comprises a quasi-periodic process, i.e. amplitude modulation of the involved harmonics is induced by the continuous – yet slow compared to the excitation time scale – change of the non-linear soil reaction.

– a memory mechanism that accounts for friction reduction at the pile–soil interface is proposed and implemented, based on the number of accumulated loading cycles. Comparison between model predictions and field data showcases the potential of the proposed shaft reaction model in the analysis of vibratory pile installation.

– the shaft friction is identified as the main mechanism of soil reaction to driving in the present case, while the pile penetration is found insensitive to variation of the plastic tip resistance. This finding is strongly dependent on the pile dimensions and for offshore monopiles it is expected to be even more apparent, given the large embedment depths required.

– the average penetration rate was found to be a monotonic function of the driving frequency, based on a numerical study conducted by means of the presented model. Field tests that focus on the effect of the driving frequency on both installation and post-installation performance are necessary to define what may constitute the optimal driving frequency.

CRediT authorship contribution statement

Athanasios Tsetas: Conceptualization, Methodology, Software, Validation, Formal analysis, Investigation, Data curation, Visualization, Writing – original draft. **Apostolos Tsouvalas:** Conceptualization, Methodology, Writing – review & editing, Supervision, Project administration, Funding acquisition. **Andrei V. Metrikine:** Conceptualization, Methodology, Writing – review & editing, Supervision, Project administration, Funding acquisition.

Declaration of competing interest

The authors declare that they have no known competing financial interests or personal relationships that could have appeared to influence the work reported in this paper.

Data availability

Some data may be made available upon reasonable request to the corresponding author, after approval of all GDP project partners.

Acknowledgements

This paper is associated with the GDP project in the framework of the GROW joint research programme. Funding from Topsector Energiesubsidie van het Ministerie van Economische Zaken, Netherlands under grant number TEHE117100 and financial/technical support from the following partners is gratefully acknowledged: Royal Boskalis Westminster N.V., Netherlands, CAPE Holland B.V., United States, Deltares, Netherlands, Delft Offshore Turbine B.V., Netherlands, Delft University of Technology, Netherlands, ECN, Netherlands, Eneco Wind B.V., Netherlands, IHC IQIP B.V., Netherlands, RWE Offshore Wind Netherlands B.V., SHL Offshore Contractors B.V., Netherlands, Shell Global Solutions International B.V., Netherlands, Sif Netherlands B.V., TNO, Netherlands, and Van Oord Offshore Wind Projects B.V, Netherlands.

Appendix A. Vibrations of cylindrical shells via the SAFE method

For $n = 0$, the SAFE mass and stiffness matrices $\mathbf{I}^l_{p,0}$ and $\mathbf{L}^l_{p,0}$ for a cylindrical shell segment l with length d_l read:

$$\mathbf{I}^l_{p,0} = 2\pi R_p h_p \begin{bmatrix} \frac{d_l}{3} & 0 & 0 & \frac{d_l}{6} & 0 & 0 \\ 0 & \frac{13d_l}{35} & \frac{11d_l^2}{210} & 0 & \frac{9d_l}{70} & -\frac{13d_l^2}{420} \\ 0 & \frac{11d_l^2}{210} & \frac{d_l^3}{105} & 0 & \frac{13d_l^2}{420} & -\frac{d_l^3}{140} \\ \frac{d_l}{6} & 0 & 0 & \frac{d_l}{3} & 0 & 0 \\ 0 & \frac{9d_l}{70} & \frac{13d_l^2}{420} & 0 & \frac{13d_l}{35} & -\frac{11d_l^2}{210} \\ 0 & -\frac{13d_l^2}{420} & -\frac{d_l^3}{140} & 0 & -\frac{11d_l^2}{210} & \frac{d_l^3}{105} \end{bmatrix} \tag{A.1}$$

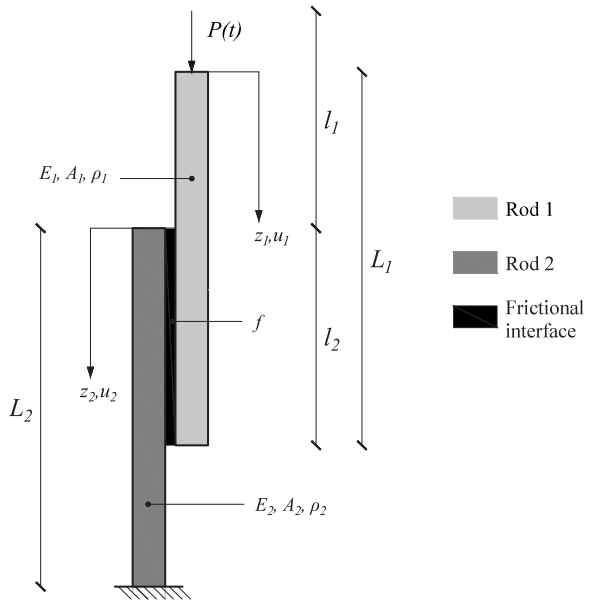

Fig. B.20. Two rods in frictional contact.

$$\mathbf{L}^{l}_{\mathrm{p},0} = 2\pi R_{\mathrm{p}} D_{\mathrm{p}} \times \begin{bmatrix} \frac{1}{d_l} & -\frac{\nu_{\mathrm{p}}}{2R_{\mathrm{p}}} & -\frac{d_l\nu_{\mathrm{p}}}{12R_{\mathrm{p}}} & -\frac{1}{d_l} & -\frac{\nu_{\mathrm{p}}}{2R_{\mathrm{p}}} & \frac{d_l\nu_{\mathrm{p}}}{12R_{\mathrm{p}}} \\ -\frac{\nu_{\mathrm{p}}}{2R_{\mathrm{p}}} & \frac{35h_{\mathrm{p}}^2R_{\mathrm{p}}^2+13d_l^4}{35d_l^3R_{\mathrm{p}}^2} & \frac{105h_{\mathrm{p}}^2R_{\mathrm{p}}^2+11d_l^4}{210d_l^2R_{\mathrm{p}}^2} & \frac{\nu_{\mathrm{p}}}{2R_{\mathrm{p}}} & \frac{-70h_{\mathrm{p}}^2R_{\mathrm{p}}^2+9d_l^4}{70d_l^3R_{\mathrm{p}}^2} & \frac{210h_{\mathrm{p}}^2R_{\mathrm{p}}^2-13d_l^4}{420d_l^2R_{\mathrm{p}}^2} \\ -\frac{d_l\nu_{\mathrm{p}}}{12R_{\mathrm{p}}} & \frac{105h_{\mathrm{p}}^2R_{\mathrm{p}}^2+11d_l^4}{210d_l^2R_{\mathrm{p}}^2} & \frac{35h_{\mathrm{p}}^2R_{\mathrm{p}}^2+d_l^4}{105d_lR_{\mathrm{p}}^2} & \frac{d_l\nu_{\mathrm{p}}}{12R_{\mathrm{p}}} & \frac{-210h_{\mathrm{p}}^2R_{\mathrm{p}}^2+13d_l^4}{420d_l^2R_{\mathrm{p}}^2} & \frac{70h_{\mathrm{p}}^2R_{\mathrm{p}}^2-3d_l^4}{420d_lR_{\mathrm{p}}^2} \\ -\frac{1}{d_l} & \frac{\nu_{\mathrm{p}}}{2R_{\mathrm{p}}} & \frac{d_l\nu_{\mathrm{p}}}{12R_{\mathrm{p}}} & \frac{1}{d_l} & \frac{\nu_{\mathrm{p}}}{2R_{\mathrm{p}}} & -\frac{d_l\nu_{\mathrm{p}}}{12R_{\mathrm{p}}} \\ -\frac{\nu_{\mathrm{p}}}{2R_{\mathrm{p}}} & \frac{-70h_{\mathrm{p}}^2R_{\mathrm{p}}^2+9d_l^4}{70d_l^3R_{\mathrm{p}}^2} & \frac{-210h_{\mathrm{p}}^2R_{\mathrm{p}}^2+13d_l^4}{420d_l^2R_{\mathrm{p}}^2} & \frac{\nu_{\mathrm{p}}}{2R_{\mathrm{p}}} & \frac{35h_{\mathrm{p}}^2R_{\mathrm{p}}^2+13d_l^4}{35d_l^3R_{\mathrm{p}}^2} & \frac{-105h_{\mathrm{p}}^2R_{\mathrm{p}}^2-11d_l^4}{210d_l^2R_{\mathrm{p}}^2} \\ \frac{d_l\nu_{\mathrm{p}}}{12R_{\mathrm{p}}} & \frac{210h_{\mathrm{p}}^2R_{\mathrm{p}}^2-13d_l^4}{420d_l^2R_{\mathrm{p}}^2} & \frac{70h_{\mathrm{p}}^2R_{\mathrm{p}}^2-3d_l^4}{420d_lR_{\mathrm{p}}^2} & -\frac{d_l\nu_{\mathrm{p}}}{12R_{\mathrm{p}}} & \frac{-105h_{\mathrm{p}}^2R_{\mathrm{p}}^2-11d_l^4}{210d_l^2R_{\mathrm{p}}^2} & \frac{35h_{\mathrm{p}}^2R_{\mathrm{p}}^2+d_l^4}{105d_lR_{\mathrm{p}}^2} \end{bmatrix} \tag{A.2}$$

where $D_{\mathrm{p}} = \frac{E_{\mathrm{p}}h_{\mathrm{p}}}{1-\nu_{\mathrm{p}}^2}$.

Appendix B. Vibrations of two elastic rods in frictional contact

Two linear homogeneous elastic rods are considered with domains $0 \le z_1 \le L_1$ and $0 \le z_2 \le L_2$, respectively (see Fig. B.20), and their equations of motion read:

$$\rho_1 A_1 \frac{\partial^2 u_1}{\partial t^2} = E_1 A_1 \frac{\partial^2 u_1}{\partial z_1^2} + f, \quad \rho_2 A_2 \frac{\partial^2 u_2}{\partial t^2} = E_2 A_2 \frac{\partial^2 u_2}{\partial z_2^2} - f \tag{B.1}$$

In Eq. (B.1), E_i, A_i, ρ_i, $u_i(z_i,t)$ denote the modulus of elasticity, the area of the cross section, the mass density per unit length and the axial displacements of the rods ($i = 1, 2$), while f is the distributed Coulomb friction force. Conclusively, the boundary conditions read as follows:

$$N_1(0,t) = -P(t), \quad N_1(L_1,t) = 0, \quad N_2(0,t) = 0, \quad u_2(L_2,t) = 0 \tag{B.2}$$

where $N_1(z_1,t)$ and $N_2(z_2,t)$ denote the axial forces of rods 1 and 2, respectively, and $P(t)$ is the external force at the top of rod 1. The governing equations of the problem have been presented herein and further details about this problem can be found in Tsetas et al. (2022b).

References

Achmus, M., Schmoor, K.A., Herwig, V., Matlock, B., 2020. Lateral bearing behaviour of vibro-and impact-driven large-diameter piles in dense sand. Geotechnik 43 (3), 147–159.

Ahmad, T., Zhang, D., 2020. A critical review of comparative global historical energy consumption and future demand: The story told so far. Energy Rep. 6, 1973–1991.

Al-Sammarraie, D., Kreiter, S., Mörz, T., Kluger, M., Goodarzi, M., 2022. VCPT: An in-situ soil investigation method to validate vibratory pile-soil interaction models. In: Cone Penetration Testing 2022. CRC Press, pp. 799–805.

Bandyopadhyay, N., Archer, R.R., 1979. Semi-analytical finite element analysis of end problems for orthotropic cylinders. Int. J. Solids Struct. 15 (11), 871–883.

Bartoli, I., Marzani, A., Di Scalea, F.L., Viola, E., 2006. Modeling wave propagation in damped waveguides of arbitrary cross-section. J. Sound Vib. 295 (3–5), 685–707.

Berghe, J.V., Holeyman, A., 2002. Application of a hypoplastic constitutive law into a vibratory pile driving model. In: Proceedings of the International Conference on Vibratory Pile Driving and Deep Soil Compaction. Transvib 2002, Louvain-la-Neuve, Belgium, pp. 61–68.

Bhattiprolu, U., Bajaj, A.K., Davies, P., 2016. Periodic response predictions of beams on nonlinear and viscoelastic unilateral foundations using incremental harmonic balance method. Int. J. Solids Struct. 99, 28–39.

Bielefeld, M., Moscoso, N., Verbeek, G., 2020. Soil modeling for pile driving simulations using a vibro hammer. In: Offshore Technology Conference. OnePetro.

Buckley, R., Kontoe, S., Jardine, R., Maron, M., Schroeder, F., Barbosa, P., 2017. Common pitfalls of pile driving resistance analysis–A case study of the Wikinger offshore windfarm. In: Proc. 8th Intl. Conf. Offshore Site Investigation and Geotechnics. pp. 1246–1253.

Byrne, T., Gavin, K., Prendergast, L., Cachim, P., Doherty, P., Pulukul, S.C., 2018. Performance of CPT-based methods to assess monopile driveability in North Sea sands. Ocean Eng. 166, 76–91.

Cameron, T., Griffin, J.H., 1989. An alternating frequency/time domain method for calculating the steady-state response of nonlinear dynamic systems. J. Appl. Mech. 56, 149—154.

Chapelle, D., Bathe, K.-J., 2010. The Finite Element Analysis of Shells-Fundamentals. Springer Science & Business Media.

Chrisopoulos, S., Vogelsang, J., 2019. A finite element benchmark study based on experimental modeling of vibratory pile driving in saturated sand. Soil Dyn. Earthq. Eng. 122, 248–260.

Collino, F., Tsogka, C., 2001. Application of the perfectly matched absorbing layer model to the linear elastodynamic problem in anisotropic heterogeneous media. Geophysics 66 (1), 294–307.

COMSOL AB, 2022. COMSOL multiphysics® v. 5.6. https://www.comsol.com.

de Oliveira Barbosa, J.M., Park, J., Kausel, E., 2012. Perfectly matched layers in the thin layer method. Comput. Methods Appl. Mech. Engrg. 217, 262–274.

Dormand, J.R., Prince, P.J., 1980. A family of embedded Runge–Kutta formulae. J. Comput. Appl. Math. 6 (1), 19–26.

Esteban, M.D., Diez, J.J., López, J.S., Negro, V., 2011. Why offshore wind energy? Renew. Energy 36 (2), 444–450.

Fontanela, F., Grolet, A., Salles, L., Hoffmann, N., 2019. Computation of quasi-periodic localised vibrations in nonlinear cyclic and symmetric structures using harmonic balance methods. J. Sound Vib. 438, 54–65.

Francois, S., Goh, H., Kallivokas, L.F., 2021. Non-convolutional second-order complex-frequency-shifted perfectly matched layers for transient elastic wave propagation. Comput. Methods Appl. Mech. Engrg. 377, 113704.

Gallezot, M., Treyssede, F., Laguerre, L., 2018. A modal approach based on perfectly matched layers for the forced response of elastic open waveguides. J. Comput. Phys. 356, 391–409.

Géradin, M., Rixen, D.J., 2014. Mechanical Vibrations: Theory and Application to Structural Dynamics. John Wiley & Sons.

Gómez, S.S., Tsetas, A., Metrikine, A.V., 2022. Energy flux analysis for quantification of vibratory pile driving efficiency. J. Sound Vib. 541, 117299.

Gómez, S.S., Tsetas, A., Tsouvalas, A., Metrikine, A.V., 2023. Dynamic pile response during vibratory driving and modal-based strain field mapping. In: International Conference on Wave Mechanics and Vibrations. Springer, pp. 1125–1134.

Gravenkamp, H., Saputra, A.A., Duczek, S., 2021. High-order shape functions in the scaled boundary finite element method revisited. Arch. Comput. Methods Eng. 28 (2), 473–494.

Holeyman, A.E., 2002. Soil behavior under vibratory driving. In: Proceedings of the International Conference on Vibratory Pile Driving and Deep Soil Compaction. Transvib 2002, pp. 3–19.

Jonker, G., 1987. Vibratory pile driving hammers for pile installations and soil improvement projects. In: Offshore Technology Conference. OnePetro.

Juhász, Z., Szekrényes, A., 2015. Progressive buckling of a simply supported delaminated orthotropic rectangular composite plate. Int. J. Solids Struct. 69, 217–229.

Kausel, E., 1981. An Explicit Solution for the Green Functions for Dynamic Loads in Layered Media. Technical Report R81-13, Publication No. 699, Department of Civil Engineering, Massachusetts Institute of Technology.

Kausel, E., 1999. Dynamic point sources in laminated media via the thin-layer method. Int. J. Solids Struct. 36 (31–32), 4725–4742.

Kausel, E., 2006. Fundamental Solutions in Elastodynamics: A Compendium. Cambridge University Press.

Kausel, E., de Oliveira Barbosa, J.M., 2012. PMLs: A direct approach. Internat. J. Numer. Methods Engrg. 90 (3), 343–352.

Kausel, E., Peek, R., 1982. Dynamic loads in the interior of a layered stratum: an explicit solution. Bull. Seismol. Soc. Am. 72 (5), 1459–1481.
Kausel, E., Roësset, J.M., 1981. Stiffness matrices for layered soils. Bull. Seismol. Soc. Am. 71 (6), 1743–1761.
Kementzetzidis, E., Pisanò, F., Elkadi, A., Tsouvalas, A., Metrikine, A., 2023. Gentle driving of piles (GDP) at a sandy site combining axial and torsional vibrations: Part II - cyclic/dynamic lateral loading tests. Ocean Eng. 270, 113452.
Kim, S., Pasciak, J., 2009. The computation of resonances in open systems using a perfectly matched layer. Math. Comp. 78 (267), 1375–1398.
Krack, M., Gross, J., 2019. Harmonic Balance for Nonlinear Vibration Problems, Vol. 1. Springer.
Krack, M., Panning-von Scheidt, L., Wallaschek, J., 2013. A high-order harmonic balance method for systems with distinct states. J. Sound Vib. 332 (21), 5476–5488.
Kucukcoban, S., Goh, H., Kallivokas, L.F., 2019. On the full-waveform inversion of Lamé parameters in semi-infinite solids in plane strain. Int. J. Solids Struct. 164, 104–119.
Kucukcoban, S., Kallivokas, L.F., 2011. Mixed perfectly-matched-layers for direct transient analysis in 2D elastic heterogeneous media. Comput. Methods Appl. Mech. Engrg. 200 (1–4), 57–76.
Laxalde, D., Thouverez, F., 2009. Complex non-linear modal analysis for mechanical systems: Application to turbomachinery bladings with friction interfaces. J. Sound Vib. 322 (4–5), 1009–1025.
Leissa, A.W., 1973. Vibration of Shells, Vol. 288. Scientific and Technical Information Office, National Aeronautics and Space Administration.
Machaček, J., Staubach, P., Tafili, M., Zachert, H., Wichtmann, T., 2021. Investigation of three sophisticated constitutive soil models: From numerical formulations to element tests and the analysis of vibratory pile driving tests. Comput. Geotech. 138, 104276.
Marques, F., Flores, P., Claro, J.P., Lankarani, H.M., 2016. A survey and comparison of several friction force models for dynamic analysis of multibody mechanical systems. Nonlinear Dynam. 86 (3), 1407–1443.
Matuszyk, P.J., 2017. Modeling of guided circumferential SH and lamb-type waves in open waveguides with semi-analytical finite element and perfectly matched layer method. J. Sound Vib. 386, 295–310.
Mazza, N., Holeyman, A., 2019. Frequency-penetration response spectrum on vibratory amplitude matching of monopiles. In: 10th International Conference on Stress Wave Theory and Testing Methods for Deep Foundations. ASTM International.
Merchant, N.D., 2019. Underwater noise abatement: economic factors and policy options. Environ. Sci. Policy 92, 116–123.
Metrikine, A.V., Tsouvalas, A., Segeren, M.L.A., Elkadi, A.S.K., Tehrani, F.S., Gómez, S.S., Atkinson, R., Pisanò, F., Kementzetzidis, E., Tsetas, A., Molenkamp, T., van Beek, K., de Vries, P., 2020. GDP: A new technology for gentle driving of (mono)piles. In: Proceedings of the 4th International Symposium on Frontiers in Offshore Geotechnics. Austin, TX, USA, 16–19 August 2020.
Moriyasu, S., Kobayashi, S., Matsumoto, T., 2018. Experimental study on friction fatigue of vibratory driven piles by in situ model tests. Soils Found. 58 (4), 853–865.
Morvaridi, M., Brun, M., 2016. Perfectly matched layers for flexural waves: An exact analytical model. Int. J. Solids Struct. 102, 1–9.
Nguyen, C.T., Tassoulas, J.L., 2018. Reciprocal absorbing boundary condition with perfectly matched discrete layers for transient analysis of SV-P waves in a layered half-space. Int. J. Solids Struct. 155, 89–108.
Papadis, E., Tsatsaronis, G., 2020. Challenges in the decarbonization of the energy sector. Energy 205, 118025.
Powell, M.J., 1970. A hybrid method for nonlinear equations. In: Numerical Methods for Nonlinear Algebraic Equations. Gordon and Breach.
Quaegebeur, S., Chouvion, B., Thouverez, F., 2022. Nonlinear dynamic analysis of three-dimensional bladed-disks with frictional contact interfaces based on cyclic reduction strategies. Int. J. Solids Struct. 236, 111277.
Ramírez, L., Fraile, D., Brindley, G., 2020. Offshore Wind in Europe: Key Trends and Statistics 2019. Technical Report, WindEurope, Brussels, Belgium.
Randolph, M., Dolwin, R., Beck, R., 1994. Design of driven piles in sand. Geotechnique 44 (3), 427–448.
Rodger, A., Littlejohn, G., 1980. A study of vibratory driving in granular soils. Géotechnique 30 (3), 269–293.
Rodrigues, S., Restrepo, C., Kontos, E., Pinto, R.T., Bauer, P., 2015. Trends of offshore wind projects. Renew. Sustain. Energy Rev. 49, 1114–1135.
Santos, H., Soares, C.M.M., Soares, C.A.M., Reddy, J., 2009. A semi-analytical finite element model for the analysis of cylindrical shells made of functionally graded materials. Compos. Struct. 91 (4), 427–432.
Schneider, J.A., Xu, X., Lehane, B.M., 2008. Database assessment of CPT-based design methods for axial capacity of driven piles in siliceous sands. J. Geotech. Geoenviron. Eng. 134 (9), 1227–1244.
Spada, A., Capriotti, M., di Scalea, F.L., 2020. Global-local model for guided wave scattering problems with application to defect characterization in built-up composite structures. Int. J. Solids Struct. 182, 267–280.
Staubach, P., Machaček, J., Skowronek, J., Wichtmann, T., 2021. Vibratory pile driving in water-saturated sand: Back-analysis of model tests using a hydro-mechanically coupled CEL method. Soils Found. 61 (1), 144–159.
Taciroglu, E., Liu, C., Dong, S., Chun, C., 2004. Analysis of laminated piezoelectric circular cylinders under axisymmetric mechanical and electrical loads with a semi-analytic finite element method. Int. J. Solids Struct. 41 (18–19), 5185–5208.
Timoshenko, S.P., Woinowsky-Krieger, S., 1959. Theory of Plates and Shells. McGraw-hill.
Treyssede, F., Nguyen, K.-L., Bonnet-BenDhia, A.-S., Hazard, C., 2014. Finite element computation of trapped and leaky elastic waves in open stratified waveguides. Wave Motion 51 (7), 1093–1107.
Tsetas, A., Gómez, S.S., Tsouvalas, A., van Beek, K., Tehrani, F.S., Kementzetzidis, E., Pisanò, F., Elkadi, A., Segeren, M., Molenkamp, T., Metrikine, A.V., 2020. Experimental identification of the dynamic behaviour of pile-soil system installed by means of three different pile-driving techniques. In: Proceedings of the XI International Conference on Structural Dynamics, Vol. II. EURODYN 2020, European Association for Structural Dynamics, pp. 3005–3015.
Tsetas, A., Tsouvalas, A., Gómez, S., Pisanò, F., Kementzetzidis, E., Molenkamp, T., Elkadi, A., Metrikine, A., 2023. Gentle driving of piles (GDP) at a sandy site combining axial and torsional vibrations: Part I - installation tests. Ocean Eng. 270, 113453.
Tsetas, A., Tsouvalas, A., Metrikine, A.V., 2021. Installation of large-diameter monopiles: introducing wave dispersion and non-local soil reaction. J. Mar. Sci. Eng. 9 (3), 313.
Tsetas, A., Tsouvalas, A., Metrikine, A.V., 2022a. An alternating frequency-time harmonic balance method for fast-slow dynamical systems. In: Proceedings of the 28th International Congress on Sound and Vibration. International Institute of Acoustics and Vibration, IIAV.
Tsetas, A., Tsouvalas, A., Molenkamp, T., Metrikine, A.V., 2022b. A mode-matching method for the prediction of stick-slip relative motion of two elastic rods in frictional contact. Acta Mech. 233 (2), 753–773.
Tsouvalas, A., 2020. Underwater noise emission due to offshore pile installation: A review. Energies 13 (12), 3037.
Tsouvalas, A., Metrikine, A.V., 2016. Structure-borne wave radiation by impact and vibratory piling in offshore installations: From sound prediction to auditory damage. J. Mar. Sci. Eng. 4 (3), 44.
Van Dorp, R., Moscoso, N., Bielefeld, M., Verbeek, G., 2019. Prediction and monitoring of installation of offshore foundation monopiles for windfarms. In: Offshore Technology Conference. OnePetro.
Waas, G., 1972. Linear Two-Dimensional Analysis of Soil Dynamics Problems in Semi-Infinite Layer Media (Ph.D. thesis). University of California.
Xiao, Y., Ge, Y., 2022. A numerical model of VPS for offshore wind turbine monopiles based on hypoplastic theory. Int. J. Numer. Anal. Methods Geomech. 46 (4), 697–716.